

Neural gradients are lognormally distributed: understanding sparse and quantized training

Brian Chmiel^{†◦*} Liad Ben-Uri^{◦*} Moran Shkolnik^{†◦} Elad Hoffer[†]
Ron Banner[†] Daniel Soudry[◦]

[†]Habana Labs – An Intel company, Caesarea, Israel,

[◦]Department of Electrical Engineering - Technion, Haifa, Israel

{bchmiel, mshkolnik, ehoffer, rbanner}@habana.ai
{liadgo2, daniel.soudry}@gmail.com

Abstract

Neural gradient compression remains a main bottleneck in improving training efficiency, as most existing neural network compression methods (e.g., pruning or quantization) focus on weights, activations, and weight gradients. However, these methods are not suitable for compressing neural gradients, which have a very different distribution. Specifically, we find that the neural gradients follow a lognormal distribution. Taking this into account, we suggest two methods to reduce the computational and memory burdens of neural gradients. The first one is stochastic gradient pruning, which can accurately set the sparsity level — up to 85% gradient sparsity without hurting validation accuracy (ResNet18 on ImageNet). The second method determines the floating-point format for low numerical precision gradients (e.g., FP8). Our results shed light on previous findings related to local scaling, the optimal bit-allocation for the mantissa and exponent, and challenging workloads for which low-precision floating-point arithmetic has reported to fail. Reference implementation accompanies the paper.

1 Introduction

Pruning and quantization are two commonly used methods to compress CNNs and make them more resource-efficient. For example, these compression methods can be applied to a trained model’s weights and activations, to improve the model’s efficiency during inference. However, using such compression methods during training is more challenging, in two aspects: (1) In order to significantly improve training efficiency we must address the computationally-intensive backward-pass, facing the compression-sensitive gradients, (2) the compression algorithm itself must be efficient, excluding, for example, the use of fine-tuning that prevails in post-training methods.

Understanding the statistical distributions of weights, activations, and gradients at different layers during the training is fundamental to their quantization and pruning. Many previous works (Banner et al., 2018b; Ye et al., 2019; Fang et al., 2020) approximate these distributions using some analytically tractable distribution (e.g. Gaussian or Laplacian distribution) and use it to analyze and optimize their proposed compression scheme.

Our key observation in this paper is that the distribution of neural gradients (also called layer gradients) is heavy-tailed, which is fundamentally different from the light-tailed distribution of the weights and activations. Specifically, when plotted at a logarithmic scale, these values approximately

*Equal contribution.

follow a normal distribution. This indicates that gradient tensors empirically follow a lognormal distribution. Statistical tests to compare the observed gradients’ distribution and the theoretical lognormal distribution are consistent with this observation. This makes exiting statistical methods to reduce the computational/memory cost of weights and activations inapplicable for neural gradients.

Adopting this lognormal observation, our paper suggests two main applications — pruning and quantization, used to reduce the computational and memory burden of neural gradients. To tackle these challenges, we first formalize the problems and find closed-form measures for sparsity and tensor distortion (relative error or cosine similarity) that depend only on the estimated lognormal parameters. These measures are easy to use and enable real-time optimization of compression hyper-parameters — based on gradient statistics during training.

First, we show how to perform *accurate and predictable stochastic pruning* of gradients on the fly while adaptively *allocating different sparsity levels* to each layer. Our scheme precisely sets the sparsity level and enables state-of-the-art sparsity levels without hurting validation accuracy. Second, we show how to find the *optimal floating-point format* to represent the wide dynamic range of gradients with the smallest possible roundoff errors. Our results provide useful insights that make empirically-based heuristics such as *loss scaling* (Micikevicius et al., 2017) a more grounded approach with a theoretical basis and improved performance. In Figure 1 we summarize these applications and how they are derived.

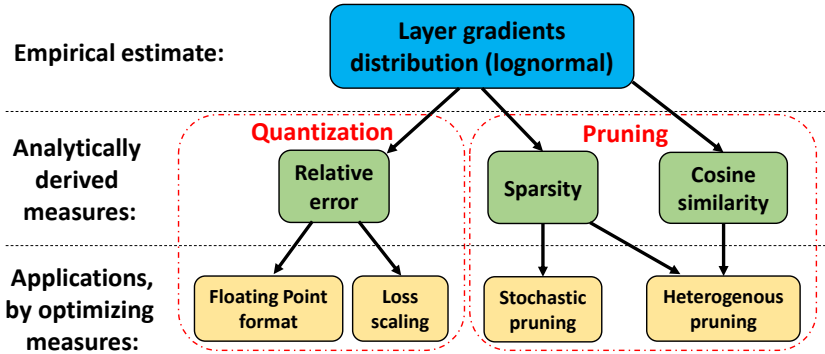


Figure 1: High-level overview of the different methods developed in this work. Adopting the lognormal observation of the neural gradients, we suggest three different analytical measures: two for pruning and one for quantization. These analytical measures are used in four different applications.

2 Related Work

Pruning - Pruning of neural networks has seen a tremendous amount of work, starting with classical methods in the late 1980s (Janowsky, 1989; Mozer & Smolensky, 1989a,b; Karnin, 1990) and amounting to dozens of papers published in recent years (Blalock et al., 2020). So far, most methods have focused on weights pruning in a post-training setup, producing models with a smaller footprint and a reduced number of FLOPs for inference in resource-constrained environments. However, these methods didn’t address the problem of the resource-intensive training of modern CNNs. More recently, methods that used pruning at initialization (Lee et al., 2019) or during training (Gale et al., 2019), while aiming to achieve sparse weights for inference, might also benefit the training itself. Focusing on the computationally-intensive back-propagation, "meProp" (Sun et al., 2017) prunes the K smallest absolute-valued entries of the neural gradients on the fly, using the top-k algorithm. Works following it, switched the pruning with quantization to induce sparsity (Wiedemann et al., 2020), or used top-k pruning as well on the copies of weights and activations used in back-prop (Aamir Raihan & Aamodt, 2020). Another method, (Ye et al., 2019) inspired by conventional unbiased estimators like stochastic rounding, suggested "stochastic pruning", reaching higher sparsity levels. Nevertheless, using this method requires finding a threshold that would yield the desired sparsity level. Trying to solve this, the authors assumed the gradients are normally distributed. This inaccurate assumption leads to an incorrect estimation of the threshold and a large difference between the required sparsity and the one obtained. This gap is bridged using an intensive hyper-parameter search — with a significant overhead occurring at each layer and each iteration.

Quantization - Quantization of neural networks has also been the topic of much recent research, aiming to reduce both bandwidth and memory footprint, as well as computation time. While a lot of research focused on the quantization of weights and activations for inference (Krishnamoorthi, 2018; Choi et al., 2018; Jain et al., 2019), there were also major advances in quantization during training, many of them faced difficulty trying to represent the high dynamic range of the gradients (Banner et al., 2018a; Wu et al., 2018). Some methods, like (Banner et al., 2018b) used a distributional assumption for the tensors involved, approximating the optimal clipping value analytically from the distribution of the tensor by minimizing the mean-square-error measure. Our work also takes a rigorous approach to approximate the optimal floating-point quantizer from the distribution of the gradients, which is different than that of the weights and activations. Bit allocation for floating-point formats has proven crucial in deep learning workloads, where for example, BF16 has shown greater success compared to traditional FP16 format due to wider dynamic range (Henry et al., 2019; Kalamkar et al., 2019). Research over required format and trade-offs in exponent versus mantissa is on-going with growing interest over lower precision representations such as FP8. Some works have explored using different FP8 formats: Wang et al. (2018) has used (1-5-2: sign-exponent-mantissa), while (Sun et al., 2019) suggests using one type of FP8 format for the forward (1-4-3), and a different FP8 format (1-5-2) for the backward pass, after empirically assessing the different possible formats. Additionally, with the growing usage of FP16 mixed-precision training (Micikevicius et al., 2017), researchers and practitioners faced the need to use loss scaling (Micikevicius et al., 2017), adjusting the tensor distribution to avoid over/under-flow. This procedure required, in some cases, an intensive parameter search and wasn't guaranteed to succeed in all cases.

3 Neural gradients distribution

Preliminaries. A neural network is a composition of different blocks that include linear and non-linear functions. In CNNs the most common block contains the trio Conv-BN-ReLU. Consider a CNN with L layers, the output, $\mathcal{A}_{i;3}$, of layer $i \in \{1, \dots, L\}$ is:

$$[\text{Conv}] \mathcal{A}_{i;1} = W_i \times \mathcal{A}_{i-1;3} \quad [\text{BN}] \mathcal{A}_{i;2} = \text{BN}_{\beta, \gamma}(\mathcal{A}_{i;1}) \quad [\text{ReLU}] \mathcal{A}_{i;3} = \max(0, \mathcal{A}_{i;2}), \quad (1)$$

where \times defines a convolution operation, W_i is the weights matrix, and BN is a batch-norm operation. The corresponding gradients are $\nabla \mathcal{A}_{i;1-3}$, ∇W_i , $\nabla \beta$ and $\nabla \gamma$ (full derivation in Appendix A.1)

Recent works (Banner et al., 2018b; Bernstein et al., 2018) use the assumption of a Gaussian distribution to fit the weights (W), activations (\mathcal{A}) and weights gradients (∇W) distribution. However, in the following we will show that a similar assumption (made by several works (Ye et al., 2019; Wiedemann et al., 2020)) regarding the neural gradients ($\nabla \mathcal{A}$) is false.

Estimating gradient distribution. We estimate the goodness of fit of the neural gradients ($\nabla \mathcal{A}_{i;3}$ and $\nabla \mathcal{A}_{i;2}$; $i \in [1..L]$) to several bell-shaped distributions. This is done by measuring the static distance (largest vertical line) between the cumulative distribution function (CDF) of the empirically observed distribution and the CDF of the reference distribution (also know as Kolmogorov-Smirnov test (Smirnov, 1948)). This static distance to each of a variety of well-known distributions is calculated for the gradients of each layer of ResNet18 during training on the ImageNet dataset, and the average of all the layers is shown in Table 1. The analysis is performed on the absolute value of the gradients, excluding the zero-valued entries. Notice that the lognormal distribution is the best fit. The PDF of a random variable X that is lognormally distributed, i.e. $\ln X \sim \mathcal{N}(\mu, \sigma^2)$, is:

$$\frac{1}{x\sigma\sqrt{2\pi}} e^{-\frac{(\ln(x)-\mu)^2}{2\sigma^2}} \quad (2)$$

Table 1: Mean (\pm std) over all layers of Kolmogorov-Smirnov test on $\nabla \mathcal{A}_{i;3}$ & $\nabla \mathcal{A}_{i;2}$; $i \in [1..L]$ of ResNet18 on ImageNet

Distribution	Laplace	Normal	Uniform	Cauchy	Logistic	Loglaplace	Lognormal
$\nabla \mathcal{A}_{i;2}$	0.32 \pm 0.11	0.36 \pm 0.1	0.77 \pm 0.1	0.38 \pm 0.1	0.4 \pm 0.15	0.06 \pm 0.03	0.04\pm0.02
$\nabla \mathcal{A}_{i;3}$	0.33 \pm 0.1	0.4 \pm 0.17	0.78 \pm 0.1	0.3 \pm 0.12	0.35 \pm 0.1	0.04 \pm 0.03	0.01\pm0.01

The distribution of $\nabla \mathcal{A}_{i;1}$ can be described as a bi-modal lognormal distribution (see example in Fig. 2 a). The two modes stem from two different components of $\nabla \mathcal{A}_{i;2}$: the left mode originates from the zero-valued elements (that are abundant because of the ReLU) and the right mode from the rest of $\nabla \mathcal{A}_{i;2}$. The emergence of the left mode is due to the small-valued $\nabla \gamma$ and $\nabla \beta$, which are the only parts left of $\nabla \mathcal{A}_{i;1}$ where $\nabla \mathcal{A}_{i;2}$ is zero (see Eq. (A.2)). The two modes can be separated and analyzed by splitting the entries of $\nabla \mathcal{A}_{i;1}$ according to the value of the same entries in $\nabla \mathcal{A}_{i;2}$ (zero or non-zero); see the results of the Kolmogorov-Smirnov test to these distributions in Table A.1 - notice each of them can best be described as a lognormal distribution. Examples can be seen in Fig. A.1.

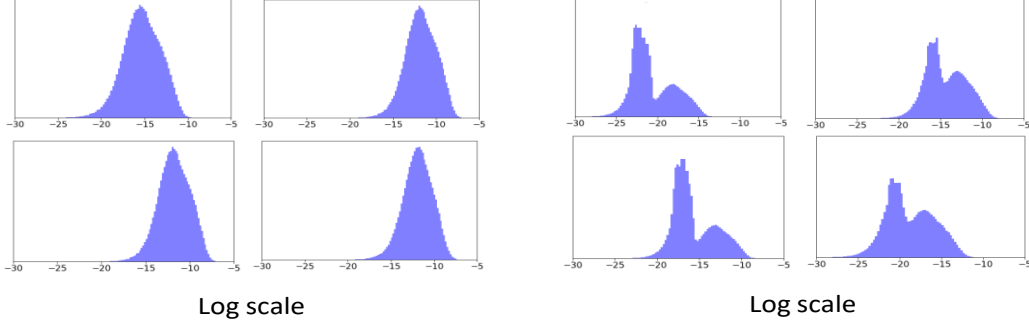


Figure 2: Histograms of $\nabla \mathcal{A}_{i;1}$ (right) and $\nabla \mathcal{A}_{i;3}$ (left) in log-scale of four layers of ResNet18 - ImageNet dataset. Histograms with additional models and datasets can be found in Appendix A.3

4 Application I - Stochastic pruning

Problem formulation. Inspired by conventional unbiased estimators for quantization such as "stochastic rounding", researchers have recently proposed "stochastic pruning" (Ye et al., 2019), an unbiased pruning method, i.e. where $\mathbb{E}(T_{\alpha,\varepsilon}(x)) = \mathbb{E}(x)$. Given a threshold α , we draw $\varepsilon \sim U[0, 1]$ and prune according to:

$$T_{\alpha,\varepsilon}(x) = \begin{cases} x & |x| > \alpha \\ \text{sign}(x) \cdot \alpha & \alpha \cdot \varepsilon \leq |x| \leq \alpha \\ 0 & |x| < \alpha \cdot \varepsilon \end{cases} \quad (3)$$

We want to find an analytical formula for obtaining a threshold α that induces the desired sparsity level S using stochastic pruning. Specifically, let X be a random variable with a known distribution and S a given sparsity level ($0 < S < 1$). Using stochastic pruning, with $\varepsilon \sim U[0, 1]$, we obtain:

$$S = \mathbb{E}_{\varepsilon} \int_0^{\alpha \cdot \varepsilon} f(x) dx \quad (4)$$

Analytical derivation of Sparsity. Understanding the lognormal distribution of the gradients, Eq. (4) is simply the CDF of a lognormal distribution at $\alpha \cdot \varepsilon$, that is:

$$S = \mathbb{E}_{\varepsilon} \left[\frac{1}{2} + \frac{1}{2} \text{erf} \left(\frac{\ln(\alpha \cdot \varepsilon) - \mu}{\sqrt{2}\sigma} \right) \right] \stackrel{\varepsilon' = \frac{\varepsilon}{e^{\mu}}}{=} \int_0^{\frac{\alpha}{e^{\mu}}} \left[\frac{1}{2} + \frac{1}{2} \text{erf} \left(\frac{\ln(\tau)}{\sqrt{2}\sigma} \right) \right] \frac{e^{\mu}}{\alpha} d\tau \quad (5)$$

The full solution for this integral can be found in Appendix A.4, resulting in:

$$S = \frac{1}{2} + \frac{e^{\mu}}{2\alpha} \left[e^{\frac{\sigma^2}{2}} \text{erf} \left(\frac{\sigma}{\sqrt{2}} - \frac{\ln(\frac{\alpha}{e^{\mu}})}{\sqrt{2}\sigma} \right) + \frac{\alpha}{e^{\mu}} \cdot \text{erf} \left(\frac{\ln(\frac{\alpha}{e^{\mu}})}{\sqrt{2}\sigma} \right) - e^{\frac{\sigma^2}{2}} \right] \quad (6)$$

Given σ, μ of the distribution and the desired sparsity S this equation can be easily solved numerically to find α . As shown in Fig. A.6 the std and mean of the gradients' distribution at each layer is quite stable throughout the training; this allows us to infrequently sample them and calculate the threshold that will be used for several backward passes, while saving the computational resources required for the computation. In practice, we perform this procedure, of measuring σ, μ and finding α , only once every epoch while achieving stable sparsity levels throughout the training. Moreover, the computational complexity of solving Eq. (6) is negligible (empirically it converges in a few iterations); further details can be found in Appendix A.5.

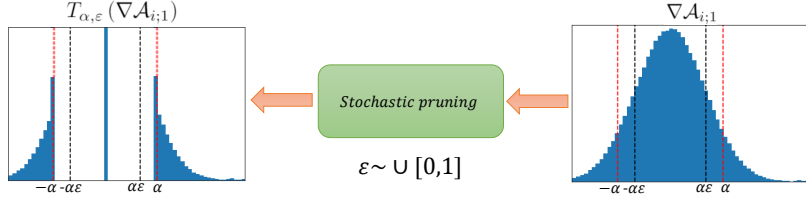


Figure 3: Effect of stochastic pruning on a lognormally distributed tensor. The threshold can be found from Eq. (4) according to the gradients’ distribution. S is the ratio of values mapped to 0, notice that a large fraction of values, all values $\alpha \cdot \varepsilon \leq x \leq \alpha$ are mapped to $\pm\alpha$ - two values that can have a special encoding, thus reducing the tensors’ memory footprint - details in Appendix A.9.

Pruning a mixture of lognormal distributions. To achieve even higher sparsity levels we can apply this method to the mixture of lognormally distributed gradients, $\nabla \mathcal{A}_{i;1}$. These gradients are comprised of two lognormal distributions with different means, variances, and number of elements. Dealing with this distribution in the same theoretical framework as was done for the lognormal distribution is challenging. However, a simple solution can allow us to apply the same results to this distribution. We will rely on the fact that most of the values in the left mode are several orders of magnitude smaller than the ones in the right mode. Hence for a large enough sparsity value, we can say the following - if we will ignore the left mode and calculate the threshold assuming only the right mode exists then for almost all of the values in the left mode $|x| < \alpha \cdot \varepsilon$ and thus will be pruned. Therefore, to achieve an overall sparsity level of S we can find the threshold using the parameters of the right mode, adjusting the desired sparsity level down to account for the elements of the left mode that would be pruned as well. Additional details in Appendix A.6. In Fig. A.2 we show that the proposed method indeed achieves the desired sparsity.

Heterogeneous sparsity allocation. We identify in Fig. A.3a that the angle between the tensors before and after the stochastic pruning, measured by the cosine similarity, as an important proxy to the overall validation accuracy achieved. Interestingly, using the cosine similarity, we observed that stochastic pruning takes a different toll from the different layers, i.e. pruning all layers to the same sparsity level damages some of them more than others. This phenomenon can be explained and assessed by analyzing the cosine similarity of a lognormal distribution, where the difference between the layers is the parameters of the distribution. We derive the cosine similarity as another analytical measure and propose an algorithm that better preserves the cosine similarity of some of the layers, by decreasing their sparsity level, while increasing the sparsity level of other layers — maintaining the overall sparsity budget (mean sparsity of all the layers). Further details can be found in Appendix A.7.1. This allows us to increase the sparsity level while preserving accuracy, results can be seen in Fig. 5a.

Encoding. High sparsity levels, achieved at high levels of threshold α by our method, can be used to significantly reduce the bandwidth used by the gradients. We suggest a custom encoding method that fully utilizes the abundance of both zeros and $\pm\alpha$ generated by the stochastic pruning, at their relative frequency. The compression ratio achieved by the proposed encoding, relative to original FP32, is equivalent to quantizing to 4 bits at 80% sparsity, and to only 2 bits at 90%. See further details in Appendix A.9.

5 Application II - Optimal Floating-Point Quantization

Floating-point (FP) representations can cover a very wide dynamic range with a relatively small number of digits. This dynamic range is especially important for the heavy-tailed distributions that characterize neural gradients. In this section, we study the optimal characteristics of the FP quantizer.

Problem formulation. We can decompose any given real value $y \in \mathbb{R}$ as follows:

$$y = \text{sgn}(y) \cdot \overbrace{|y|}^{x \in \mathbb{R}^+}; \quad x = 2^{\ln x} = \overbrace{2^{\ln x - \lfloor \ln x \rfloor}}^{M \in [1, 2)} \cdot \overbrace{2^{\lfloor \ln x \rfloor}}^{E \in \mathbb{Z}} \quad (7)$$

Where $M \in [1, 2)$ is the mantissa and $E \in \mathbb{Z}$ the exponent. Given N bits, we use 1 bit for $\text{sgn}(y)$ and seek the optimal allocation of n_1 bits to M and n_2 bits to E , s.t. $n_1 + n_2 = N - 1$. We define the quantized x_q as:

$$x_q = \begin{cases} 2^{E_{\max}} & E \geq E_{\max} \\ M_q \cdot 2^E & -E_{\max} \leq E \leq E_{\max} \\ 0 & E \leq -E_{\max} \end{cases} \quad (8)$$

Where $E_{\max} = 2^{n_2-1}$ and M_q is the quantized mantissa with the range $[1, 2)$ divided into 2^{n_1} quantization levels with a spacing of $\Delta = \frac{1}{2^{n_1}}$. We also define the relative error as:

$$\eta(n_1, n_2) = \left| \frac{x_q - x}{x} \right| \quad (9)$$

Analytical derivation of the relative error. We assume that $x \sim \text{Lognormal}(\mu, \sigma^2)$. Note that $E = \lfloor \ln x \rfloor \approx \ln x \sim \mathcal{N}(\mu, \sigma^2)$. In Appendix A.11 we split the range into three parts according to E : (i) $-E_{\max} \leq E \leq E_{\max}$; (ii) $E \geq E_{\max}$; (iii) $E \leq -E_{\max}$, and calculate the expected contribution for each term, and establish the following closed-form expression for the expected relative error.

$$E[\eta(n_1, n_2)] = \frac{2\Phi\left(\frac{E_{\max}}{\sigma}\right) - 1}{8 \cdot \ln(2) \cdot (2^{n_1} - 1)} + 2^{E_{\max}-1} e^{\frac{\sigma^2 \ln^2(2)}{2}} \left(\text{erf}\left(\frac{\sigma \ln 2}{\sqrt{2}} + \frac{E_{\max}}{\sqrt{2}\sigma}\right) - 1 \right) + \quad (10)$$

$$- \frac{1}{2} \text{erf}\left(\frac{E_{\max}}{\sqrt{2}\sigma}\right) + \frac{3}{2} - \Phi\left(\frac{E_{\max}}{\sigma}\right)$$

where $\Phi(x)$ is the CDF of $\mathcal{N}(0, 1)$. In Fig. 4a we show that analytical results stated by Eq. (10) are in good agreement with simulations for FP8 with various number of exponent bits. Simulations were obtained by quantizing 10,000 values, generated from a lognormal distribution with $\sigma = 1, 3, 5$.

The optimal mantissa-exponent representation. The relative error in Eq. 10 depends on the scale parameter σ , and n_1 & n_2 , the number of bits of the mantissa and exponent, respectively (the latter through $E_{\max} = 2^{n_2-1}$). Given any N -bit FP format, seek a mantissa-exponent partition that minimizes the expected relative error such that $n_1 + n_2 = N - 1$. Minimizing Eq. 10 yields this optimal partition. To do so we set $n_1 = N - n_2 - 1$, equate the derivative to zero and solve. The computational cost of such a solution is negligible (details are in Appendix A.11.4). This allocation depends on N and σ . In Fig. 4b we show the optimal allocations for $N = 5, 6, 7, 8$ bits and $\sigma \in [1, 8]$.

In Fig. 4c and Fig. A.6b we show that σ has a range of $[3, 5.5]$ and $[2.5, 4.5]$ in ImageNet and Cifar100 datasets respectively, which we use to determine the optimal mantissa-exponent partition for FP5–FP8. Specifically, the analysis indicates that the optimal allocation is 4 bits for the exponent for FP5, and either 4 or 5 bits for FP6–FP8 on ImageNet (Cifar100 is the same, except it allocates 4 bits for FP6-7). Whenever there are two or more optimal allocations in the specified range (e.g., FP7 & FP8), we observe that the larger exponent allocation is preferred. This translates into an optimal FP format of 1-4-0 (sign-exponent-mantissa) for FP5, 1-5-0 for FP6 (1-4-1 in Cifar100), 1-5-1 for FP7 (1-4-2 in Cifar100), and 1-5-2 for FP8. This matches the previously suggested allocation for FP8 (Sun et al., 2019). In Section 6, we use these partitions to train ImageNet and Cifar models at reduced precision (bit-width lower than 8), and prove empirically that these partitions provide the best results.

Adjusting the loss scaling. The use of loss scaling (Micikevicius et al., 2017), is key to the quantization of gradients using low precision FP formats. The idea is to reduce the dynamic range of the neural gradients to fit the floating-point range and then rescale again for the weights update. Choosing a fixed global loss scale that can fit all the layers is challenging and in some cases impossible. The solution usually comes from using a dynamic loss scale, which changes if it encounters under/over-flow in the weights update, and actually updating the weights only if there is no under/over-flow.

This method becomes more challenging for more aggressive quantization levels (that reduce the dynamic range) and in more complicated networks (e.g transformers (Vaswani et al., 2017)). In

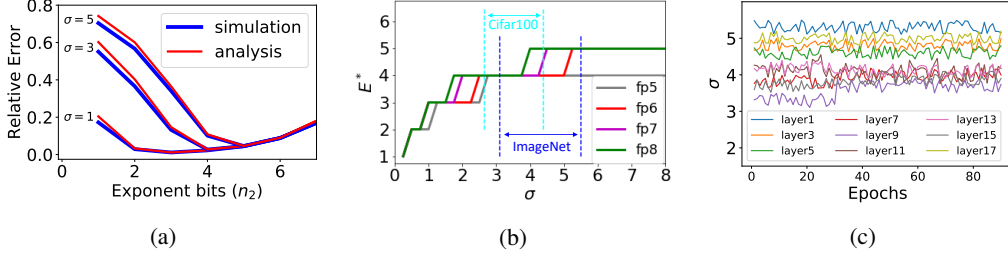


Figure 4: **(a)** Expected relative error as a function of n_2 for FP8. The simulation is in good agreement with the analytical results stated by Eq. (10). **(b)** Ideal bit allocation for the exponent (E^*) as a function of σ , using Eq. (10). Notice that σ varies between datasets, imposing different optimal allocation. **(c)** σ of different layers throughout training (ResNet18 on ImageNet).

Fig. A.7 we show the std of the lognormally distributed gradients in different layers of a transformer (Vaswani et al., 2017), notice the high variability in the std between layers, that makes the choice of one global loss scale very challenging. The variation in gradient statistics across layers may also explain the need for previous hybrid approaches, where some layers were intentionally kept at high precision. For example, Sun et al. (2019) reported that for FP8 training of a ResNet models, they had to keep both the first and last layers at FP16 precision. In Fig. A.8, we demonstrate that this constraint may stem from the different statistics of the first and last layers, which may require a different scaling to remedy.

Based on the lognormal distribution of the gradients we suggest to use a layer-wise logarithmic loss scaling, which is equivalent to the subtraction of the mean before quantization of a Normally distributed tensor (Banner et al., 2018b). Given a neural gradient X we define $\mu_l = \frac{1}{N} \sum_i \log_2(x_i)$, N being the dimension of X . Then we normalize the neural gradient, $X_{\text{norm}} = X/2^{\mu_l}$. X_{norm} can then be quantized using a floating-point format. The next neural gradient and weight gradient need to be restored to the correct scale, i.e. be multiplied by the same factor 2^{μ_l} to maintain the magnitudes as in FP32 training. As shown in Fig. A.6 the mean of the gradients' distribution at each layer is quite stable throughout the training; this allows us to infrequently sample them.

6 Experiments

In this section, we evaluate the methods and predictions above, all stemming from the lognormal distribution of the neural gradients, for the two suggested applications: stochastic pruning and floating point format quantization. Experiments, details, and additional results appear in Appendix A.12.

Stochastic pruning. In Fig. 5a we compare the proposed methods for homogeneous and heterogeneous stochastic pruning against SAW (Aamir Raihan & Aamodt, 2020) that uses "top-k" pruning and ATP (Ye et al., 2019) that also uses stochastic pruning but assumes the gradients are normally distributed. Notice that stochastic pruning outperforms the non-stochastic top-k, and that the heterogeneous version surpasses the homogeneous one. The validation accuracy during training for different sparsity levels and different datasets can be found in Fig. A.11. In Fig. 5b we demonstrate our methods' ability to produce the required sparsity level, for both the homogeneous and heterogeneous versions. This is not achieved neither by finding the threshold using top-k and then applying stochastic pruning, nor by using ATP (Ye et al., 2019), which assumes a normal distribution. In Fig. A.10 it shows that this occurs also when examining the sparsity of each layer individually. this strengthens the importance of using the correct distribution of the neural gradients in Eq. (4).

Floating point format. In Table 2 we show results of different allocations between exponent and mantissa for different FP formats in Cifar100 and ImageNet dataset. We quantize all convolutional layers' gradients, unlike previous methods (Sun et al., 2019) that keep part of them in FP32. All results were achieved using the suggested layer-wise loss scaling, where the mean is sampled once every epoch. For all FP formats, the results fit the analysis, which predicts the best results for FP6, FP7 in ImageNet to be 1-5-0 (sign-exponent-mantissa) and 1-5-1 respectively, and for FP5 and FP6 in Cifar100 1-4-0 and 1-4-1, respectively.

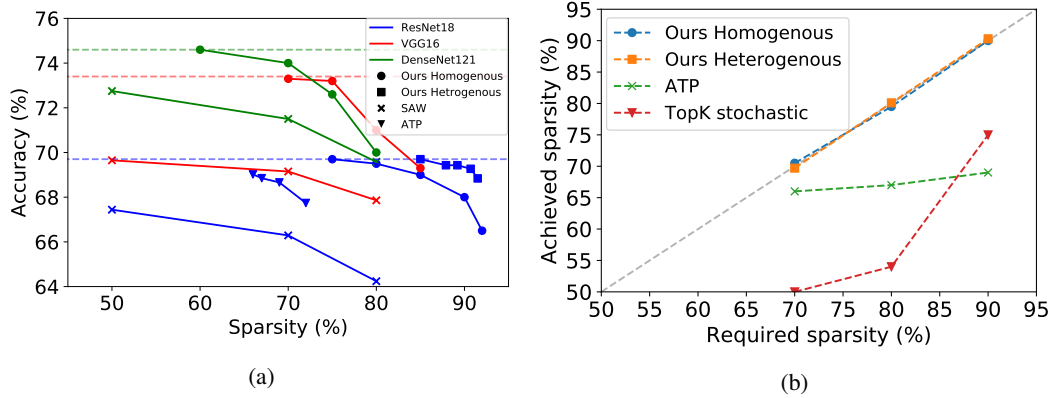


Figure 5: **(a)** Comparison of the homogeneous and heterogeneous stochastic pruning methods against pruning with SAW (Aamir Raihan & Aamodt, 2020), which uses the "top-k" method and ATP (Ye et al., 2019), which also uses stochastic pruning, but assumes the neural gradients are Normally distributed. These are compared on 3 different architectures (ResNet18, VGG16 and DenseNet121). Our proposed methods achieve higher sparsity while maintaining base-line validation accuracy. **(b)** Comparison of the required and achieved sparsity of our method, ATP (Ye et al., 2019) and applying "top-k" followed by stochastic pruning. The validation accuracy for our method is never less than the accuracy of the other methods for same achieved sparsity. Notice the large deviation in the other methods between the achieved and required sparsity. This emphasizes the importance of using the correct distribution in order to both enjoy the improved performance of stochastic pruning over regular "top-k", and maintain the ability to fully control the achieved sparsity. Additional details and results are in Appendix A.12

Table 2: Floating-point formats for neural gradient representations. The table reports the validation accuracy of ResNet18 on ImageNet & Cifar100, and ResNet101 on Cifar100. E^* denotes the optimal exponent bit-width, which minimizes the expected relative error of Eq. (10). N/A refers to cases of invalid format (e.g., 1-5-0 is the optimal FP6 format for ImageNet, but FP6 cannot have $E^* + 1 = 6$ exponent bits). Note that in all cases, the formats that are predicted by Eq. (10) to minimize the relative error also provide the highest accuracies (**bolded**).

Dataset	Model	Range of σ	Baseline	FP	E^*	E^*+1	E^*-1	E^*-2
Cifar100	ResNet18	2.5 - 4.5	64.9%	FP5	64.0%	N/A	58.9%	26.6%
				FP6	64.9%	64.6%	59.7%	28.6%
	ResNet101	2.5-4.5	71.3%	FP5	70.4%	N/A	66.5%	35%
				FP6	70.97%	70.82%	67.5%	42.7%
ImageNet	ResNet18	3 - 5.5	70.4%	FP6	70.0%	N/A	67.1%	30.8%
				FP7	70.4%	70.1%	66.7%	47.5%

7 Summary

We evaluate the distribution of neural gradients and show they can best be modeled as a lognormal distribution. We use this distribution to analytically derive accurate measures (e.g. sparsity and local distortion metrics), which are useful for the following applications.

Pruning. We are able to use stochastic pruning to prune the neural gradients during training precisely to a predetermined sparsity level, with minimal overhead computation. We show that this form of stochastic pruning is superior to deterministic pruning. Specifically, we achieve up to 80% gradient sparsity without hurting validation accuracy (ResNet18 on ImageNet) using a homogeneous sparsity level for all layers. We also show that the uniform sparsity method is sub-optimal with respect to an analytical error measure we derive, the cosine similarity, and suggest to allocate different sparsity levels to the different layers in order to better preserve it. We suggest and test an algorithm for this allocation - allowing for more aggressive overall pruning, achieving 85% gradient sparsity while preserving baseline accuracy, and reaching nearly 90% with less than 0.3% accuracy degradation.

Quantization. We find the optimal bit allocation to the mantissa and exponent for a floating point gradient representation, which explains prior results for FP8 and paves the way towards lower accuracy representations. We suggest using a per-layer loss scale and find the optimal value for it, preventing under/over-flow in scenarios that challenged prior methods or required an intensive parameter search. Combining both methods, we trained using low precision neural gradients on ImageNet and achieved, for the first time, no noticeable validation accuracy degradation with FP7, and a degradation of just 0.4% with FP6.

Broader impact

Training deep learning models is an energy intensive process. Recent articles (Strubell et al., 2019) estimate that the carbon footprint of training one model is as much as 284 tonnes of carbon dioxide, equivalent to 5 times the lifetime emissions of an average car. Recent methods of quantization or pruning are able to reduce the energy footprint by x8 or even more, with minimal degradation in performance. This energy reduction helps us address the issue of global warming, while still enjoying the benefits of modern deep learning methods.

References

- Md Aamir Raihan and Tor M. Aamodt. Sparse weight activation training. *arXiv:2001.01969*, 2020.
- Ron Banner, Itay Hubara, Elad Hoffer, and Daniel Soudry. Scalable methods for 8-bit training of neural networks. In *NeurIPS*, 2018a.
- Ron Banner, Yury Nahshan, Elad Hoffer, and Daniel Soudry. Post-training 4-bit quantization of convolution networks for rapid-deployment. *arXiv preprint arXiv:1810.05723*, 2018b. URL <http://arxiv.org/abs/1810.05723>.
- Chaim Baskin, Natan Liss, Yoav Chai, Evgenii Zheltonozhskii, Eli Schwartz, Raja Girayes, Avi Mendelson, and Alexander M Bronstein. Nice: Noise injection and clamping estimation for neural network quantization. *arXiv preprint arXiv:1810.00162*, 2018. URL <http://arxiv.org/abs/1810.00162>.
- Jeremy Bernstein, Yu-Xiang Wang, Kamyar Azizzadenesheli, and Anima Anandkumar. signsgd: compressed optimisation for non-convex problems. In *ICML*, 2018.
- Gerard Biau and David M Mason. High-dimensional norms. In *Mathematical Statistics and Limit Theorems*, pp. 21–40. Springer, 2015.
- Davis Blalock, Jose Javier Gonzalez Ortiz, Jonathan Frankle, and John Gutttag. What is the state of neural network pruning?, 2020.
- Jungwook Choi, Pierce I-Jen Chuang, Zhuo Wang, Swagath Venkataramani, Vijayalakshmi Srinivasan, and Kailash Gopalakrishnan. Bridging the accuracy gap for 2-bit quantized neural networks (qnn), 2018.
- Jia Deng, Wei Dong, Richard Socher, Li-Jia Li, Kai Li, and Li Fei-Fei. Imagenet: A large-scale hierarchical image database. In *2009 IEEE conference on computer vision and pattern recognition*, pp. 248–255. Ieee, 2009.
- Jun Fang, Ali Shafiee, Hamzah Abdel-Aziz, David Thorsley, Georgios Georgiadis, and Joseph Hassoun. Post-training piecewise linear quantization for deep neural networks. *arXiv: Computer Vision and Pattern Recognition*, 2020.
- Trevor Gale, Erich Elsen, and Sara Hooker. The state of sparsity in deep neural networks, 2019.
- Kaiming He, Xiangyu Zhang, Shaoqing Ren, and Jian Sun. Deep residual learning for image recognition. *2016 IEEE Conference on Computer Vision and Pattern Recognition (CVPR)*, pp. 770–778, 2016.
- Greg Henry, Ping Tak Peter Tang, and Alexander Heinecke. Leveraging the bfloat16 artificial intelligence datatype for higher-precision computations. In *2019 IEEE 26th Symposium on Computer Arithmetic (ARITH)*, pp. 69–76. IEEE, 2019.

- C. A. R. Hoare. Algorithm 65: Find. *Commun. ACM*, 4(7):321–322, July 1961. ISSN 0001-0782. doi: 10.1145/366622.366647. URL <https://doi.org/10.1145/366622.366647>.
- Gao Huang, Zhuang Liu, and Kilian Q. Weinberger. Densely connected convolutional networks. *2017 IEEE Conference on Computer Vision and Pattern Recognition (CVPR)*, pp. 2261–2269, 2017.
- Sambhav R. Jain, Albert Gural, Michael Wu, and Chris H. Dick. Trained quantization thresholds for accurate and efficient fixed-point inference of deep neural networks, 2019.
- S. A. Janowsky. Pruning versus clipping in neural networks. *Physical Review A*, 39(12):6600–6603, 1989. URL <https://link.aps.org/doi/10.1103/PhysRevA.39.6600>.
- Dhiraj Kalamkar, Dheevatsa Mudigere, Naveen Mellempudi, Dipankar Das, Kunal Banerjee, Sasikanth Avancha, Dharmaraja Teja Vooturi, Nataraj Jammalamadaka, Jianyu Huang, Hector Yuen, et al. A study of bfloat16 for deep learning training. *arXiv preprint arXiv:1905.12322*, 2019.
- E. D. Karnin. A simple procedure for pruning backpropagation trained neural networks. *IEEE transactions on neural networks*, 1(2):239–242, 1990.
- Raghuraman Krishnamoorthi. Quantizing deep convolutional networks for efficient inference: A whitepaper, 2018.
- Namhoon Lee, Thalaiyasingam Ajanthan, Stephen Gould, and Philip H. S. Torr. A signal propagation perspective for pruning neural networks at initialization, 2019.
- Paulius Micikevicius, Sharan Narang, Jonah Alben, Gregory Frederick Diamos, Erich Elsen, David García, Boris Ginsburg, Michael Houston, Oleksii Kuchaiev, Ganesh Venkatesh, and Hao Wu. Mixed precision training. *ArXiv*, abs/1710.03740, 2017.
- M. C. Mozer and P. Smolensky. Skeletonization: A technique for trimming the fat from a network via relevance assessment. *Advances in neural information processing systems*, pp. 107–115, 1989a.
- M. C. Mozer and P. Smolensky. Using relevance to reduce network size automatically. *Connection Science*, 1(1):3–16, 1989b.
- Karen Simonyan and Andrew Zisserman. Very deep convolutional networks for large-scale image recognition. *CoRR*, abs/1409.1556, 2015.
- N. Smirnov. Table for estimating the goodness of fit of empirical distributions. *Ann. Math. Statist.* 19 (1948), no. 2, 279–281., 1948. URL <https://projecteuclid.org/euclid.aoms/1177730256>.
- Emma Strubell, Ananya Ganesh, and Andrew McCallum. Energy and policy considerations for deep learning in nlp, 2019.
- Xiao Sun, Jungwook Choi, Chia-Yu Chen, Naigang Wang, Swagath Venkataramani, Vijayalakshmi Srinivasan, Xiaodong Cui, Wei Zhang, and Kailash Gopalakrishnan. Hybrid 8-bit floating point (hfp8) training and inference for deep neural networks. In *NeurIPS*, 2019.
- Xu Sun, Xuancheng Ren, Shuming Ma, and Houfeng Wang. meprop: Sparsified back propagation for accelerated deep learning with reduced overfitting. *arXiv:1706.06197*, 2017.
- Ashish Vaswani, Noam Shazeer, Niki Parmar, Jakob Uszkoreit, Llion Jones, Aidan N. Gomez, Lukasz Kaiser, and Illia Polosukhin. Attention is all you need. *ArXiv*, abs/1706.03762, 2017.
- Naigang Wang, Jungwook Choi, Daniel Brand, Chia-Yu Chen, and Kailash Gopalakrishnan. Training deep neural networks with 8-bit floating point numbers, 2018.
- Simon Wiedemann, Temesgen Mehari, Kevin Kepp, and Wojciech Samek. Dithered backprop: A sparse and quantized backpropagation algorithm for more efficient deep neural network training, 2020.
- Shuang Wu, Guoqi Li, Feng Chen, and Luping Shi. Training and inference with integers in deep neural networks, 2018.
- Xucheng Ye, Jianlei Yang, Pengcheng Dai, Yiran Chen, and Weisheng Zhao. Accelerating cnn training by sparsifying activation gradients. *arXiv:1908.00173*, 2019.

A Supplementary Material

A.1 CNN gradients

$$[\text{ReLU}] \quad \nabla \mathcal{A}_{i;2} = \nabla \mathcal{A}_{i;3} \cdot \delta(A_{i;2} > 0) \quad (\text{A.1})$$

$$[\text{BN}] \quad \nabla \mathcal{A}_{i;1} = \frac{\gamma_i}{\sqrt{\sigma_i^2 + \epsilon}} \left[\nabla \mathcal{A}_{i;2} - \frac{1}{N} \left(\nabla \gamma \left(\frac{\mathcal{A}_{i;1} - \mu_i}{\sqrt{\sigma_i^2 + \epsilon}} \right) + \nabla \beta \right) \right] \quad (\text{A.2})$$

$$\nabla \beta = \sum (\nabla \mathcal{A}_{i;2}) \quad \nabla \gamma = \sum \left(\nabla \mathcal{A}_{i;2} \times \frac{\mathcal{A}_{i;1} - \mu_i}{\sqrt{\sigma_i^2 + \epsilon}} \right)$$

$$[\text{Conv}] \quad \nabla \mathcal{A}_{i-1;3} = \nabla \mathcal{A}_{i;1} \times W_i^T \quad \nabla W_i = \nabla \mathcal{A}_{i;1} \times \mathcal{A}_{i-1;3} \quad (\text{A.3})$$

A.2 Mixture of log-Normal distribution

The distribution of $\nabla \mathcal{A}_{i;1}$ can be approximated as a bi-modal lognormal distribution. The two modes stem from two different components of $\nabla \mathcal{A}_{i;2}$: the left mode originates from the zero-valued elements (that are abundant because of the ReLU) and the right mode from the rest of $\nabla \mathcal{A}_{i;2}$. We split the elements of $\nabla \mathcal{A}_{i;1}$ according to the value of the same element in $\nabla \mathcal{A}_{i;2}$ (zero or non-zero), then apply in each of them Kolmogorov-Smirnov test.

The two modes can be separated and analyzed by splitting the entries of $\nabla \mathcal{A}_{i;1}$ according to the value of the same entries in $\nabla \mathcal{A}_{i;2}$ (zero or non-zero); see the results of the Kolmogorov-Smirnov test to these distributions in Table A.1 - notice each of them can best be described as a lognormal distribution. Examples can be seen in Fig. A.1.

To estimate $\nabla \mathcal{A}_{i;1}$, we divide the data of $\nabla \mathcal{A}_{i;2}$ to zero and non-zero elements. Then, we apply Kolmogorov-Smirnov test (Smirnov, 1948) to each of them, and show in Table A.1 they fit to lognormal distribution - obtaining a total of bi modal lognormal distribution in $\nabla \mathcal{A}_{i;1}$.

Table A.1: Mean (\pm std) over all layers of Kolmogorov-Smirnov test on $\nabla \mathcal{A}_{i;1}$ over the zero and non zero elements of $\nabla \mathcal{A}_{i;2}$ ResNet18 on ImageNet

Distribution	Laplace	Normal	Uniform	Cauchy	Logistic	Loglaplace	Lognormal
zeros	0.43 \pm 0.13	0.41 \pm 0.09	0.93 \pm 0.19	0.44 \pm 0.12	0.53 \pm 0.13	0.1 \pm 0.03	0.08\pm0.03
non-zeros	0.48 \pm 0.11	0.49 \pm 0.13	0.86 \pm 0.09	0.43 \pm 0.11	0.51 \pm 0.14	0.04 \pm 0.012	0.02\pm0.01

A.3 Histograms

In Fig. A.1 we show histograms of $\nabla \mathcal{A}_{i;1}$ divided to the zero and non-zero elements from $\nabla \mathcal{A}_{i;2}$ in ResNet18, ImageNet which as shown in Appendix A.2 each of them fit to lognormal distribution. Additionally we show histograms of different layers of Transformer (Vaswani et al., 2017), DenseNet121 and Vgg16 which at log-scale following to Normal distribution.

A.4 From sparsity to the threshold — the full solution

$$S = \mathbb{E}_\varepsilon \left[\frac{1}{2} + \frac{1}{2} \operatorname{erf} \left(\frac{\ln(\alpha \cdot \varepsilon) - \mu}{\sqrt{2}\sigma} \right) \right] \Big|_{\varepsilon' = \frac{\varepsilon}{e^\mu}} = \int_0^{\frac{\alpha}{e^\mu}} \left[\frac{1}{2} + \frac{1}{2} \operatorname{erf} \left(\frac{\ln(\tau)}{\sqrt{2}\sigma} \right) \right] \frac{e^\mu}{\alpha} d\tau$$

$$= \frac{1}{2} + \frac{e^\mu}{2\alpha} \left[e^{\frac{\sigma^2}{2}} \operatorname{erf} \left(\frac{\sigma^2 - \ln(\tau)}{\sqrt{2}\sigma} \right) + \tau \operatorname{erf} \left(\frac{\ln(\tau)}{\sqrt{2}\sigma} \right) \right] \Big|_0^{\frac{\alpha}{e^\mu}} \quad (\text{A.4})$$

$$= \frac{1}{2} + \frac{e^\mu}{2\alpha} \left[e^{\frac{\sigma^2}{2}} \operatorname{erf} \left(\frac{\sigma}{\sqrt{2}} - \frac{\ln(\frac{\alpha}{e^\mu})}{\sqrt{2}\sigma} \right) + \frac{\alpha}{e^\mu} \cdot \operatorname{erf} \left(\frac{\ln(\frac{\alpha}{e^\mu})}{\sqrt{2}\sigma} \right) - e^{\frac{\sigma^2}{2}} \right]$$

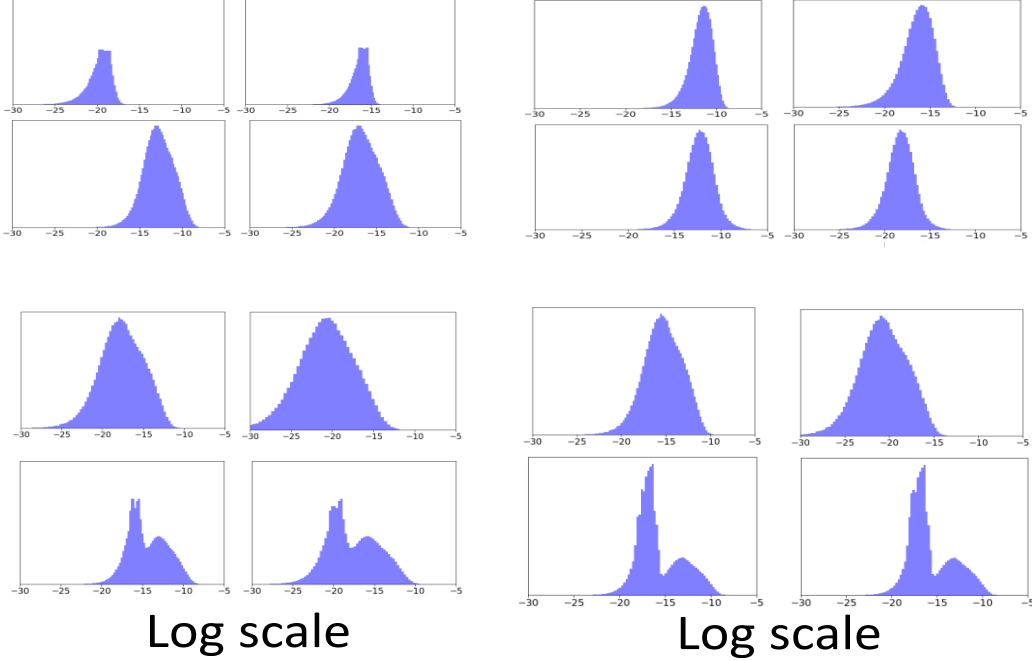


Figure A.1: **(Top left)** $\nabla \mathcal{A}_{i;1}$ distribution divided to the two components of $\nabla \mathcal{A}_{i;2}$ in two different layers. The left mode (top) originates from the zero element of $\nabla \mathcal{A}_{i;2}$ and the right mode (bottom) from the non zero elements, ResNet18 on ImageNet. **(Top right)** Histograms of neural gradients in different layers of Transformer (Vaswani et al., 2017) for WMT’16 En-De dataset in the decoder attention layer (top) and encoder embedding (bottom). **(Bottom left)** Histograms of neural gradients in different layers of DensNet121, ImageNet dataset. **(Bottom right)** Histograms of neural gradients in different layers of Vgg16, ImageNet dataset.

A.5 Stochastic pruning complexity

The suggested stochastic pruning method solution requires the mean and standard deviation of the input — each operation has a complexity of $\mathcal{O}(n)$ for an input size n . In practice, we perform this procedure of measuring the mean and standard deviation once every epoch. Additionally, it requires the solution of Eq. (6) which is independent in the input size. We empirically found it converges in a few iterations. In total, we found that the process of obtaining a threshold α , for a required sparsity adds less than 5% to the iteration time (for the single iteration, once in an epoch, when we calculate the threshold). For rest of the iterations there is no overhead caused by the stochastic pruning, while achieving a significant improvement because of the induced sparsity.

We can compare our method with top-k, which requires every iteration $\mathcal{O}(n \log n)$ for a naive implementation (sorting) and can be reduced using quick-select (Hoare, 1961) as was proposed by (Aamir Raihan & Aamodt, 2020) and vary between $\mathcal{O}(n)$ and $\mathcal{O}(n^2)$.

A.6 Algorithm for bi-Modal lognormal pruning

Pruning of the bi-modal gradients ($\nabla \mathcal{A}_{i;1}$) is crucial for reducing the computational and bandwidth overhead. This is especially because it is involved in the calculation of the next layer gradient ($\nabla \mathcal{A}_{i-1;3}$) and weights gradients of the convolution (∇W_i). Unlike $\nabla \mathcal{A}_{i;2}$, which naturally has a high sparsity level induced by the ReLU, $\nabla \mathcal{A}_{i;1}$ is naturally not sparse at all. In the following we explain how to find the threshold α which induces the required sparsity ratio S in the bi-modal lognormal gradient.

In order to achieve a sparsity level S we use the following procedure — (1) calculate the ratio of the gradients that are in the left mode, denoted l , this is done by dividing the amount of values that were zero in the gradient before ($\nabla \mathcal{A}_{i;2}$) by the total number of elements in the gradient. (2) Here

we assume that S is large enough, i.e. $l < S$. thus in order to achieve a total sparsity of S out of the entire tensor we need to sparsity $S' = \frac{S-l}{1-l}$ of the right mode. (3) Calculate the mean μ and variance σ of the right mode, by taking only the values in the tensor that their corresponding values in the pre-BN gradients are non-zero. (4) Solve the equation to find the threshold using σ and S' and apply stochastic pruning to the entire tensor using it.

We found that for high values of sparsity, above 0.7, the method is very accurate and achieves the desired sparsity thorough-out the training. For lower sparsity levels the actual sparsity induced tends to be a bit lower because the threshold is lower and the assumption that all of the values in the left mode are zeroed deteriorates progressively as the sparsity level decreases. In Fig. A.2 we show that the proposed method indeed achieves the desired sparsity

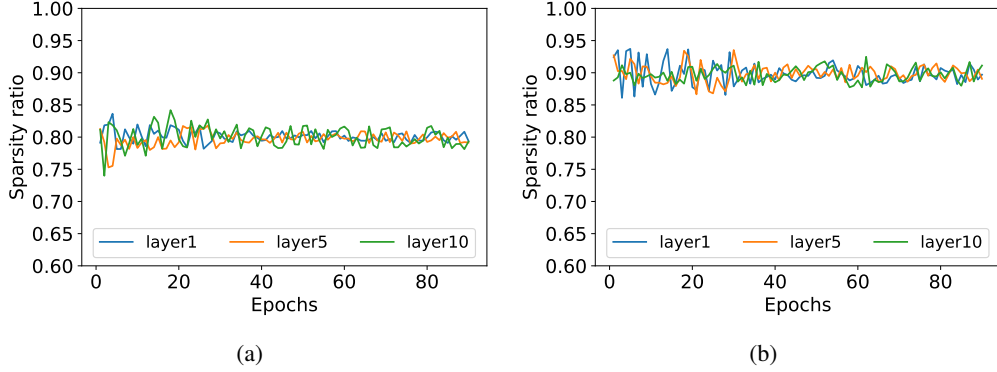


Figure A.2: The obtained sparsity in different layers of ResNet-18 with ImageNet dataset for required sparsity of 80% (a) and 90% (b)

A.7 Cosine similarity and heterogeneous stochastic pruning

A.7.1 Cosine similarity of stochastic pruning - general

Given a vector of gradients X , we would like to measure the cosine similarity (cosine of the angle) between the vector before and after stochastic pruning, i.e. X and $T_{\alpha,\varepsilon}(x)$:

$$\cos(\theta) = \frac{X \cdot T_{\alpha,\varepsilon}(x)}{\|X\|_2 \cdot \|T_{\alpha,\varepsilon}(x)\|_2} \quad (\text{A.5})$$

At high dimensions, the relative error made by substituting $\|X\|$ with $E\|X\|$ becomes asymptotically negligible (Biau & Mason, 2015). This distance concentration phenomenon simplifies Eq. A.5:

$$\cos(\theta) \approx \frac{\mathbb{E}[X \cdot T_{\alpha,\varepsilon}(X)]}{\mathbb{E}\|X\|_2 \cdot \mathbb{E}\|T_{\alpha,\varepsilon}(x)\|_2} \quad (\text{A.6})$$

Solving the different components of eq. A.6 for $X \sim \text{lognormal}(0, \sigma^2)$ with a maximum value of $k\sigma$ (regarding the maximum value see Appendix A.7.4) with n elements, we get (see Appendix A.8):

$$\mathbb{E}[X \cdot T_{\alpha,\varepsilon}(X)] = \frac{1}{2}n \cdot e^{2\sigma^2} \left[1 + \text{erf} \left(\frac{k\sigma - 2\sigma^2}{\sigma\sqrt{2}} \right) \right] \quad (\text{A.7})$$

$$\begin{aligned} \mathbb{E}\|T_{\alpha,\varepsilon}(X)\|_2^2 &= \frac{1}{2}n \cdot \alpha \cdot e^{\frac{\sigma^2}{2}} \left[1 - \text{erf} \left(\frac{\sigma^2 - \ln(\alpha)}{\sigma\sqrt{2}} \right) \right] \\ &+ \frac{1}{2}n \cdot e^{2\sigma^2} \left[\text{erf} \left(\frac{k\sigma - 2\sigma^2}{\sigma\sqrt{2}} \right) - \text{erf} \left(\frac{\ln(\alpha) - 2\sigma^2}{\sigma\sqrt{2}} \right) \right] \end{aligned} \quad (\text{A.8})$$

$$\mathbb{E}\|X\|_2^2 = \frac{1}{2}n \cdot e^{2\sigma^2} \left[1 + \text{erf} \left(\frac{k\sigma - 2\sigma^2}{\sigma\sqrt{2}} \right) \right] \quad (\text{A.9})$$

Fig. A.4 shows that these analytical results are in agreement with our simulations. We notice in Fig. A.3a that the cosine similarity between original and pruned neural gradients can be used as a proxy for validation accuracy degradation under stochastic pruning. Interestingly, in Fig. A.3b we show that using the cosine similarity, we observed that stochastic pruning takes a different toll from the different layers i.e. pruning all layers to the same sparsity level damages some of them more than others. We propose an algorithm that using the analytical measured cosine similarity (Eq. (A.7), Eq. (A.8), Eq. (A.9)) preserves the cosine similarity of some of the layers, by decreasing their sparsity level, while increasing the sparsity level of other layers — maintaining the overall sparsity budget (mean sparsity of all the layers). The motivation for that and the algorithm are described in Appendix A.7.2 and Appendix A.7.3.

A.7.2 Heterogeneous stochastic pruning

Using stochastic pruning, we noticed that different layers, with different distributional parameters, seem to be more sensitive to high levels of sparsity. This sensitivity can affect the overall accuracy achieved by the network. We notice two important parameters that contribute to the sensitivity of the layer: (1) its depth in the network, and (2) the error it suffers at a given sparsity level. The depth of the layer in the network is important because if a layer is deeper (closer to the output) then corrupting its gradients will cause the gradients reaching lower levels (closer to the input) to be corrupted as well. So, corruption of the gradients of the first layer, for example, affects only the first layer itself, while corrupting the gradients of the second layer affect both its gradients and the first layer’s gradients, etc. To measure the distortion of the tensor due to the pruning, we used the cosine similarity (see definition in Eq. (A.5)) between the tensor before and after the stochastic pruning process. This measure reflects the preservation of the angle of the high-dimensional gradients tensor, under the pruning process. We noticed that in our homogeneous pruning scheme though all layers had the same desired sparsity level and a very similar achieved sparsity, the cosine similarity varied significantly between the layers. This is seen clearly in Fig. A.3b where each layer has a fairly stable cosine similarity that might be very different than the other layers, this is similar to the stability of each layer’s distributional parameters that also vary between layers. In fact, as observed in Fig. A.13, the variance in cosine similarity between the layers can be explained exactly by the variance in the distributional parameters, for example the std σ .

A.7.3 Heterogeneous algorithm

While the effect of each layer’s pruning on the overall outcome (accuracy) stems from its depth in the network and its distortion (measured through cosine similarity) its contribution to the overall sparsity is controlled by the number of its elements and its sparsity level. Since we aim to maximize the overall sparsity while preserving the baseline accuracy, we propose using different sparsity levels for the different layers. This would allow us to preserve the cosine similarity of the deeper layers, that affect the gradients of more layers, while raising the sparsity of lower levels to maintain the overall sparsity. This can be done effectively because for most architectures the number of elements in the neural gradients of deeper layers is lower than these of shallow layers (usually because of max-pooling). This allows us to lower the sparsity of deeper layers significantly while raising the sparsity of shallower ones only slightly, and still preserve the overall sparsity.

We propose an algorithm in which the user determines the overall desired sparsity and the minimum cosine similarities for the L' deepest layers, which can change from layer to layer. When determining each layer’s threshold (at the beginning of each epoch, as in the regular homogeneous algorithm) if the layer is in the L' deepest layers the algorithm checks if its expected cosine similarity is greater than the minimum cosine similarity defined for that layer. If it is not, then the threshold is decreased so to achieve the minimum cosine similarity defined for that layer. After going through the L' deepest layers, that are first in the backward-pass, we know what was the sparsity for each layer so far. because we preserved the cosine similarity, the sparsity of these layers is expected to be lower than the required overall sparsity. In order to compensate for that we can set a higher sparsity level for the rest of the layers, for which we don’t define a minimum cosine similarity. This higher sparsity level can be calculated based on the sparsity of the first L' layers, which we already know, and the total number of elements in them compared to the rest of the layers.

In order to refrain from over-pruning the shallow layers we set a maximum sparsity level for the layers for which we don’t set a minimum cosine similarity level. From our experiments we find that setting

a maximum of 0.96-0.98 will prevent over-pruning of these layers, that might deteriorate the final accuracy. Of course, using this maximum sparsity while aiming for both very high overall sparsity levels and high minimum cosine similarity for many of the layers might prevent us from reaching the desired overall sparsity. However for most use-cases this doesn't pose significant restrictions on the parameters and at worse causes fairly small changes in overall sparsity.

Typical values we use to achieve high sparsity levels while preserving baseline accuracy are 0.95-0.98 minimum cosine similarity for the higher layers, where usually the deeper layers will receive higher minimum cosine similarities. For example, using ResNet18 on ImageNet, we have 4 basic blocks, we might preserve the last two with a minimum cosine similarity of 0.98 and the second one with 0.95, leaving the first block and the single layer before it, to compensate by having a higher sparsity level. In Fig. A.14 we show an example of the different sparsity levels between the different layers when using heterogeneous pruning on ResNet18 trained on ImageNet.

A.7.4 Neural gradients lognormal distributions are truncated

When evaluating the cosine similarity of the different layers we noticed that the cosine similarity measure is very sensitive to the large valued components of the tensor, that is, pruning the same tensor after removing a few of the largest magnitude components will cause a far lower cosine similarity at the same sparsity level. This is because the cosine similarity represents the change in high-dimensional angle, that is governed by the largest components.

Having first developed the equations in Appendix A.7.1 for a general lognormal distribution, we found a significant discrepancy between the expected and actual cosine similarities. That lead us to the understanding that the neural gradients' distributions actually differ slightly from the lognormal distribution by the lack of high-valued components in the abundance that we might expect from tensors of their size where each value is drawn from a lognormal distribution. We verified and quantified this observation by examining the Gumbel distribution, that models the distribution of the maximum obtained from drawing a certain number of samples from a base distribution, in this case the lognormal distribution. We found that in fact the maximum values of the gradients were significantly lower than the ones expected from the Gumbel distribution of the corresponding lognormal distribution and size of the tensor. In Fig. A.17 we show examples of the actual maximum values of the tensors compared to the expected values using the Gumbel distribution.

Finally we re-modelled the distribution of the gradients as a truncated lognormal distribution, that does not receive values above a certain value, denoted as k times the std σ . The value k is obtained from the distribution itself, like σ and μ . We found that taking the estimating k as the maximum of the obtained tensor makes a very noisy estimator, and does not match the actual cosine similarity closely, so in practice we take a high quantile (for example 0.997) of the distribution. It is important to note that this slight difference from the lognormal distribution is highly important when calculating the cosine similarity, but is negligible when dealing with sparsity, for example, because it is not sensitive to the lack of a few high-valued components.

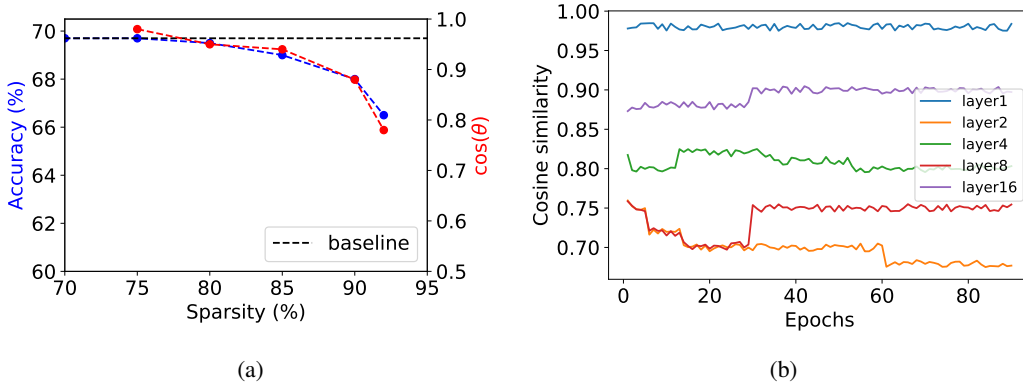


Figure A.3: (a) ResNet18 validation accuracy on the ImageNet data-set for different sparsity levels and the mean of the cosine similarity between the pruned and original gradient, notice the high correlation between the two. (b) The cosine similarity in different layers of ResNet18 on Imagenet dataset for 92 % pruning. Notice the variability between the different layers.

A.8 Cosine Similarity of Stochastic pruning - full derivation

In this section we extend on the full derivation of the cosine similarity for stochastic pruning.

To calculate the expected similarity between the n -dimensional tensors X and $T_{\alpha,\varepsilon}(X)$, we need to calculate $\mathbb{E}[X \cdot T(X)]$, $\mathbb{E}\|X\|_2$, and $\mathbb{E}\|T_{\alpha,\varepsilon}(X)\|_2$, as follows:

$$\mathbb{E}[X \cdot T_{\alpha,\varepsilon}(X)] = \mathbb{E}\left[\sum_i x_i \cdot T_{\alpha,\varepsilon}(x_i)\right] = \sum_i \mathbb{E}[x_i \cdot T_{\alpha,\varepsilon}(x_i)] = n \cdot \mathbb{E}[x \cdot T_{\alpha,\varepsilon}(x)] \quad (\text{A.10})$$

And similiary:

$$\mathbb{E}\|X\|_2 = n \cdot \mathbb{E}[x]^2 \quad (\text{A.11})$$

$$\mathbb{E}\|T_{\alpha,\varepsilon}(X)\|_2 = n \cdot \mathbb{E}[T_{\alpha,\varepsilon}(x)]^2 \quad (\text{A.12})$$

Assuming $X \sim \text{LogNormal}(0, \sigma^2)$ with maximum value $k\sigma$, the cosine similarity between X and $T_{\alpha,\varepsilon}(X)$ is :

$$\mathbb{E}\|X\|_2^2 = \frac{1}{2}n \cdot e^{2\sigma^2} \left[1 + \text{erf}\left(\frac{\ln(k\sigma) - 2\sigma^2}{\sigma\sqrt{2}}\right)\right] \quad (\text{A.13})$$

$$\begin{aligned} \mathbb{E}\|T(X)\|_2^2 &= n \int_0^1 \int_{\varepsilon\alpha}^\alpha \alpha^2 \cdot f(x) dx d\varepsilon + n \int_\alpha^{k\sigma} x^2 \cdot f(x) dx \\ &= n \int_0^1 \int_{\varepsilon\alpha}^\alpha \frac{\alpha^2}{x\sigma\sqrt{2\pi}} e^{-\frac{\ln(x)^2}{2\sigma^2}} dx d\varepsilon + n \int_\alpha^{k\sigma} \frac{x}{\sigma\sqrt{2\pi}} e^{-\frac{\ln(x)^2}{2\sigma^2}} dx \\ &= \frac{1}{2}n \cdot \alpha^2 \int_0^1 \left[\text{erf}\left(\frac{\ln(\alpha)}{\sigma\sqrt{2}}\right) - \text{erf}\left(\frac{\ln(\varepsilon\alpha)}{\sigma\sqrt{2}}\right) \right] d\varepsilon \\ &\quad + \frac{1}{2}n \cdot e^{2\sigma^2} \left[\text{erf}\left(\frac{\ln(k\sigma) - 2\sigma^2}{\sigma\sqrt{2}}\right) - \text{erf}\left(\frac{\ln(\alpha) - 2\sigma^2}{\sigma\sqrt{2}}\right) \right] \\ &= \frac{1}{2}n \cdot \alpha^2 \cdot \text{erf}\left(\frac{\ln(\alpha)}{\sigma\sqrt{2}}\right) \\ &\quad - \frac{1}{2}n \cdot \left[\alpha \cdot e^{\frac{\sigma^2}{2}} \text{erf}\left(\frac{\sigma^2 - \ln(\varepsilon\alpha)}{\sigma\sqrt{2}}\right) + \alpha^2 \varepsilon \cdot \text{erf}\left(\frac{\ln(\varepsilon\alpha)}{\sigma\sqrt{2}}\right) \right] \Big|_0^1 \\ &\quad + \frac{1}{2}n \cdot e^{2\sigma^2} \left[\text{erf}\left(\frac{\ln(k\sigma) - 2\sigma^2}{\sigma\sqrt{2}}\right) - \text{erf}\left(\frac{\ln(\alpha) - 2\sigma^2}{\sigma\sqrt{2}}\right) \right] \\ &= \frac{1}{2}n \cdot \alpha^2 \cdot \text{erf}\left(\frac{\ln(\alpha)}{\sigma\sqrt{2}}\right) \\ &\quad - \frac{1}{2}n \cdot \left[\alpha \cdot e^{\frac{\sigma^2}{2}} \text{erf}\left(\frac{\sigma^2 - \ln(\alpha)}{\sigma\sqrt{2}}\right) + \alpha^2 \cdot \text{erf}\left(\frac{\ln(\alpha)}{\sigma\sqrt{2}}\right) - \alpha \cdot e^{\frac{\sigma^2}{2}} \right] \\ &\quad + \frac{1}{2}n \cdot e^{2\sigma^2} \left[\text{erf}\left(\frac{\ln(k\sigma) - 2\sigma^2}{\sigma\sqrt{2}}\right) - \text{erf}\left(\frac{\ln(\alpha) - 2\sigma^2}{\sigma\sqrt{2}}\right) \right] \\ &= \frac{1}{2}n \cdot \alpha \cdot e^{\frac{\sigma^2}{2}} \left[1 - \text{erf}\left(\frac{\sigma^2 - \ln(\alpha)}{\sigma\sqrt{2}}\right) \right] \\ &\quad + \frac{1}{2}n \cdot e^{2\sigma^2} \left[\text{erf}\left(\frac{\ln(k\sigma) - 2\sigma^2}{\sigma\sqrt{2}}\right) - \text{erf}\left(\frac{\ln(\alpha) - 2\sigma^2}{\sigma\sqrt{2}}\right) \right] \end{aligned} \quad (\text{A.14})$$

$$\begin{aligned}
\mathbb{E}[X \cdot T(X)] &= n \int_0^1 \int_{\varepsilon\alpha}^{\alpha} \alpha \cdot x \cdot f(x) dx d\varepsilon + n \int_{\alpha}^{k\sigma} x^2 \cdot f(x) dx \\
&= \int_0^1 \int_{\varepsilon\alpha}^{\alpha} \frac{\alpha}{\sigma\sqrt{2\pi}} e^{-\frac{\ln(x)^2}{2\sigma^2}} dx d\varepsilon + n \int_{\alpha}^{k\sigma} \frac{x}{\sigma\sqrt{2\pi}} e^{-\frac{\ln(x)^2}{2\sigma^2}} dx \\
&\stackrel{y=\ln(x)}{=} n \int_0^1 \int_{\ln(\varepsilon\alpha)}^{\ln(\alpha)} \frac{\alpha}{\sigma\sqrt{2\pi}} e^{-\frac{y^2}{2\sigma^2}} e^y dy d\varepsilon + n \int_{\ln(\alpha)}^{\ln(k\sigma)} \frac{1}{\sigma\sqrt{2\pi}} e^{-\frac{y^2}{2\sigma^2}} e^{2y} dy \\
&= n \int_0^1 \int_{\ln(\varepsilon\alpha)}^{\ln(\alpha)} \frac{\alpha}{\sigma\sqrt{2\pi}} e^{-\frac{(y-\sigma^2)^2}{2\sigma^2}} e^{\frac{\sigma^2}{2}} dy d\varepsilon + n \int_{\ln(\alpha)}^{\ln(k\sigma)} \frac{1}{\sigma\sqrt{2\pi}} e^{-\frac{(y-2\sigma^2)^2}{2\sigma^2}} e^{2\sigma^2} dy \\
&= n \cdot \alpha \cdot e^{\frac{\sigma^2}{2}} \cdot \frac{1}{2} \int_0^1 \left(1 + \operatorname{erf} \left(\frac{y - \sigma^2}{\sigma\sqrt{2}} \right) \right) \Big|_{\ln(\varepsilon\alpha)}^{\ln(\alpha)} d\varepsilon \\
&\quad + n \cdot e^{2\sigma^2} \cdot \frac{1}{2} \left(1 + \operatorname{erf} \left(\frac{y - 2\sigma^2}{\sigma\sqrt{2}} \right) \right) \Big|_{\ln(\alpha)}^{\ln(k\sigma)} \\
&= \frac{1}{2} n \cdot e^{\frac{\sigma^2}{2}} \cdot \alpha \int_0^1 \left[\operatorname{erf} \left(\frac{\ln(\alpha) - \sigma^2}{\sigma\sqrt{2}} \right) - \operatorname{erf} \left(\frac{\ln(\varepsilon\alpha) - \sigma^2}{\sigma\sqrt{2}} \right) \right] d\varepsilon \\
&\quad + \frac{1}{2} n \cdot e^{2\sigma^2} \left[\operatorname{erf} \left(\frac{\ln(k\sigma) - 2\sigma^2}{\sigma\sqrt{2}} \right) - \operatorname{erf} \left(\frac{\ln(\alpha) - 2\sigma^2}{\sigma\sqrt{2}} \right) \right] \\
&= \frac{1}{2} n \cdot e^{\frac{\sigma^2}{2}} \cdot \alpha \cdot \operatorname{erf} \left(\frac{\ln(\alpha) - \sigma^2}{\sigma\sqrt{2}} \right) \\
&\quad - \frac{1}{2} n \cdot e^{\frac{\sigma^2}{2}} \left[e^{\frac{3\sigma^2}{2}} \operatorname{erf} \left(\frac{2\sigma^2 - \ln(\alpha\varepsilon)}{\sqrt{2}\sigma} \right) - \alpha\varepsilon \cdot \operatorname{erf} \left(\frac{\sigma^2 - \ln(\varepsilon\alpha)}{\sqrt{2}\sigma} \right) \right] \Big|_0^1 \\
&\quad + \frac{1}{2} n \cdot e^{2\sigma^2} \left[\operatorname{erf} \left(\frac{\ln(k\sigma) - 2\sigma^2}{\sigma\sqrt{2}} \right) - \operatorname{erf} \left(\frac{\ln(\alpha) - 2\sigma^2}{\sigma\sqrt{2}} \right) \right] \\
&= \frac{1}{2} n \cdot e^{\frac{\sigma^2}{2}} \cdot \alpha \cdot \operatorname{erf} \left(\frac{\ln(\alpha) - \sigma^2}{\sigma\sqrt{2}} \right) \\
&\quad - \frac{1}{2} n \cdot e^{\frac{\sigma^2}{2}} \left[e^{\frac{3\sigma^2}{2}} \operatorname{erf} \left(\frac{2\sigma^2 - \ln(\alpha)}{\sqrt{2}\sigma} \right) - \alpha \cdot \operatorname{erf} \left(\frac{\sigma^2 - \ln(\alpha)}{\sqrt{2}\sigma} \right) - e^{\frac{3\sigma^2}{2}} \right] \\
&\quad + \frac{1}{2} n \cdot e^{2\sigma^2} \left[\operatorname{erf} \left(\frac{\ln(k\sigma) - 2\sigma^2}{\sigma\sqrt{2}} \right) - \operatorname{erf} \left(\frac{\ln(\alpha) - 2\sigma^2}{\sigma\sqrt{2}} \right) \right] \\
&= \frac{1}{2} n \cdot e^{2\sigma^2} \left[1 - \operatorname{erf} \left(\frac{2\sigma^2 - \ln(\alpha)}{\sqrt{2}\sigma} \right) \right] \\
&\quad + \frac{1}{2} n \cdot e^{2\sigma^2} \left[1 - \operatorname{erf} \left(\frac{\ln(\alpha) - 2\sigma^2}{\sigma\sqrt{2}} \right) \right] \\
&= \frac{1}{2} n \cdot e^{2\sigma^2} \left[1 + \operatorname{erf} \left(\frac{\ln(k\sigma) - 2\sigma^2}{\sigma\sqrt{2}} \right) \right]
\end{aligned} \tag{A.15}$$

A.9 Encoding

We suggest a custom encoding method that fully utilizes the abundance of both zeros and $\pm\alpha$ generated by the stochastic pruning, at their relative frequency. As shown in Fig. A.5a the compression ratio achieved by the proposed encoding, relative to original FP32, is equivalent to quantizing to 4 bits at 80% sparsity, and to only 2 bits at 90%. In Fig. A.5b we show the actual bits per value for the results shown in Fig. 5a using the proposed encoding.

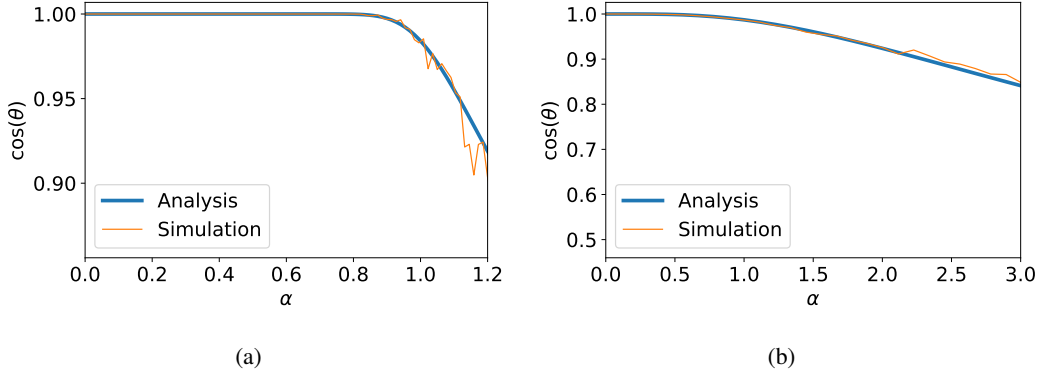


Figure A.4: Comparison between simulation and analysis (Eq. (A.7), Eq. (A.8) and Eq. (A.9)) of the cosine similarity for $\sigma = 3$ (a) and $\sigma = 5$ (b).

Table A.2: Simple proposed encoding for the values after stochastic pruning

Value	encoding
0	0
α	100
$-\alpha$	101
starting a FP value	11

A.10 Layer gradients stability

Measure of mean and std in log scale of the layer gradients in ResNet18, cifar100 dataset is shown in Fig. A.6. Notice the stability inside each epoch, that allows to sample them once in an epoch to calculate the corresponding threshold.

A.11 Floating point - relative error

We assume that $x \sim \text{Lognormal}(\mu, \sigma^2)$. Note that $E = \lfloor \ln x \rfloor \approx \ln x \sim \mathcal{N}(\mu, \sigma^2)$. We split the range into three parts according to E : (i) $-E_{\max} \leq E \leq E_{\max}$; (ii) $E \geq E_{\max}$; (iii) $E \leq -E_{\max}$, and calculate the expected contribution for each term of the relative error in Eq. (9):

A.11.1 The case of $-E_{\max} \leq E \leq E_{\max}$

In this case E can be expressed and no distortion appears due to clipping i.e., $E = E_q$. Therefore, the only contribution related to $\eta(n_1, n_2)$ is due to the distortion in the mantissa. This distortion is expressed through an additive noise $m_q = m + \varepsilon$, where the noise has a uniform distribution $\varepsilon \sim \mathcal{U}[-\Delta/2, \Delta/2]$. We can then calculate the expected relative error as follows

$$\begin{aligned}
 E \left[\left| \frac{x_q - x}{x} \right|, -E_{\max} \leq E \leq E_{\max} \right] &= E \left[\left| \frac{m \cdot 2^E - m_q \cdot 2^{E_q}}{m \cdot 2^E} \right|, -E_{\max} \leq E \leq E_{\max} \right] \\
 &= E \left[\left| \frac{m \cdot 2^E - (m + \varepsilon) \cdot 2^E}{m \cdot 2^E} \right|, -E_{\max} \leq E \leq E_{\max} \right] \\
 &= E \left[\frac{|\varepsilon|}{m} \right] = E \left(\frac{|\varepsilon|}{|m|} \right) = E|\varepsilon| \cdot E \left[\frac{1}{|m|} \right]
 \end{aligned}$$

The last factorization is permissible since ε is independent of m . The expectation of $|\varepsilon|$ in the range $[-\Delta/2, \Delta/2]$ is calculated as follows:

$$E|\varepsilon| = \int_{-\frac{\Delta}{2}}^{\frac{\Delta}{2}} \frac{|\varepsilon|}{\Delta} \cdot d\varepsilon = \frac{\varepsilon \cdot |\varepsilon|}{2\Delta} \Big|_{-\frac{\Delta}{2}}^{\frac{\Delta}{2}} = \frac{|\Delta|}{4} = \frac{1}{4 \cdot (2^{n_1} - 1)} \quad (\text{A.16})$$

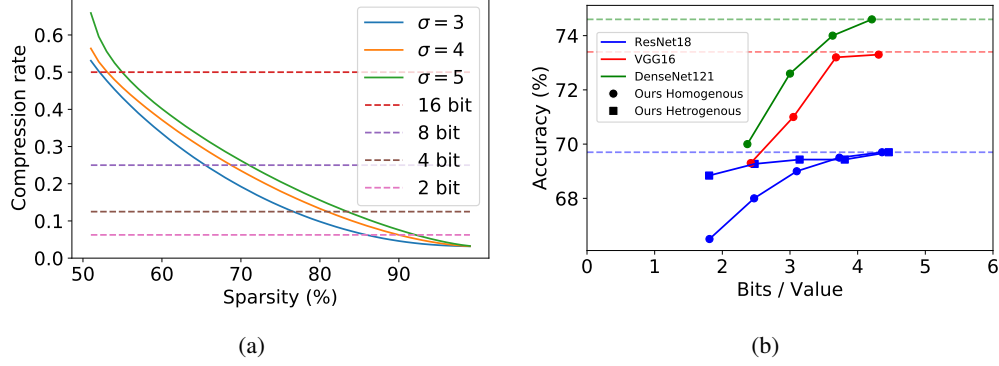


Figure A.5: (a) Compression rate achieved for the proposed encoding for a synthetic lognormal distributed tensor for common gradients σ and the comparison to quantization to different bitwidth. Notice for 90% sparsity the compression rate is similar to quantization to 2 bits. (b) Bits for each value using the proposed encoding method for the results in Fig. 5.

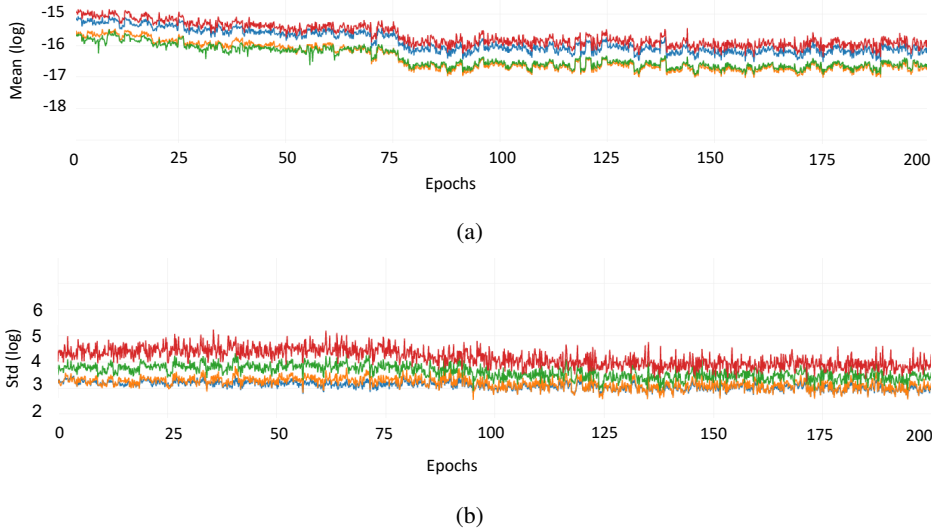


Figure A.6: The gradients mean (a) and std (b) of ResNet-18 , Cifar100 dataset in different layers. Notice they are stable across each epoch - so there is the possibility to calculate the threshold for the required sparsity once in an epoch

We turn to establish $E \left| \frac{1}{m} \right|$. Given a real value $x \in \mathbb{R}^+$, by definition m is positive and thus can be expressed as follows:

$$\left| \frac{1}{m} \right| = \frac{1}{m} = \frac{1}{2^{\ln x - \lfloor \ln x \rfloor}} = \frac{1}{2^{\varepsilon_m}} \quad (\text{A.17})$$

where ε_m can be treated as a uniform variable in the range $[0,1]$. Therefore, we have that

$$E \left| \frac{1}{m} \right| = \int_0^1 \frac{1}{2^{\varepsilon_m}} \cdot d\varepsilon = -\frac{1}{\ln(2) \cdot 2^x} \Big|_0^1 = -\frac{1}{\ln(2) \cdot 2} \approx 0.721 \quad (\text{A.18})$$

We can finally state the expected relative error for the case where x is supported by the dynamic range of x_q

$$E \left[\left| \frac{x_q - x}{x} \right|, -E_{\max} \leq E \leq E_{\max} \right] = \frac{1}{8 \cdot \ln(2) \cdot (2^{n_1} - 1)} \quad (\text{A.19})$$

We turn to find the probability $P(-E_{\max} \leq E \leq E_{\max})$. Assuming the log-Normal distribution of x we get:

$$\begin{aligned} P(-E_{\max} \leq E \leq E_{\max}) &= \Phi\left(\frac{E_{\max}}{\sigma}\right) - \Phi\left(\frac{-E_{\max}}{\sigma}\right) \\ &= 2\Phi\left(\frac{E_{\max}}{\sigma}\right) - 1 \end{aligned} \quad (\text{A.20})$$

where $\Phi(x)$ is the cumulative distribution function of the standard normal distribution.

A.11.2 The case of $E \geq E_{\max}$

$$\begin{aligned} E \left[\left| \frac{x_q - x}{x} \right|, E \geq E_{\max} \right] \cdot P(E \geq E_{\max}) &= \\ &= \int_{E_{\max}}^{\infty} \frac{2^E - 2^{E_{\max}}}{2^E} \cdot \frac{1}{\sqrt{2\pi}\sigma} e^{-\frac{E^2}{2\sigma^2}} dE \\ &= \frac{1}{2} \operatorname{erf}\left(\frac{E}{\sqrt{2}\sigma}\right) - 2^{E_{\max}-1} e^{\frac{\sigma^2 \ln^2(4)}{8}} \operatorname{erf}\left(\frac{E}{\sqrt{2}\sigma} + \frac{\sigma \ln(4)}{\sqrt{8}}\right) \Big|_{E_{\max}}^{\infty} \\ &= 2^{E_{\max}-1} e^{\frac{\sigma^2 \ln^2(2)}{2}} \left(\operatorname{erf}\left(\frac{\sigma \ln 2}{\sqrt{2}} + \frac{E_{\max}}{\sqrt{2}\sigma}\right) - 1 \right) + \\ &\quad - \frac{1}{2} \operatorname{erf}\left(\frac{E_{\max}}{\sqrt{2}\sigma}\right) + \frac{1}{2} \end{aligned} \quad (\text{A.21})$$

A.11.3 The case of $E \leq -E_{\max}$

This is the underflow case. Here we have by definition that $x_q = 0$ and therefore we get

$$E \left[\left| \frac{x_q - x}{x} \right|, E \leq -E_{\max} \right] = E \left[\left| \frac{0 - x}{x} \right|, E \leq -E_{\max} \right] = 1 \quad (\text{A.22})$$

This case has a probability of $P(E \leq -E_{\max}) = \Phi\left(-\frac{E_{\max}}{\sigma}\right) = 1 - \Phi\left(\frac{E_{\max}}{\sigma}\right)$

A.11.4 Final Expected Relative Error

Combining the three terms we have that

$$\begin{aligned} E \left[\left| \frac{x_q - x}{x} \right| \right] &= \frac{2\Phi\left(\frac{E_{\max}}{\sigma}\right) - 1}{8 \cdot \ln(2) \cdot (2^{n_1} - 1)} + 2^{E_{\max}-1} e^{\frac{\sigma^2 \ln^2(2)}{2}} \left(\operatorname{erf}\left(\frac{\sigma \ln 2}{\sqrt{2}} + \frac{E_{\max}}{\sqrt{2}\sigma}\right) - 1 \right) + \\ &\quad - \frac{1}{2} \operatorname{erf}\left(\frac{E_{\max}}{\sqrt{2}\sigma}\right) + \frac{3}{2} - \Phi\left(\frac{E_{\max}}{\sigma}\right) \end{aligned} \quad (\text{A.23})$$

Given any N -bit FP format, seek a mantissa-exponent partition that minimizes the expected relative error such that $n_1 + n_2 = N - 1$. Minimizing Eq. (A.23) yields this optimal partition. To do so we set $n_1 = N - n_2 - 1$, equate the derivative to zero and solve. Empirically we found the computational cost of such solution is negligible and can be done online without affecting the NN running time.

Moreover, we can notice that for small values of σ a lognormal distributed tensor is similar to a Normal distributed tensor. In such cases the minimization of the relative error in Eq. (A.23) induced to allocate 0 bits to the exponent, i.e fixed point quantization. This fit to previous results (Banner et al., 2018b; Baskin et al., 2018) which shows impressive results by quantization the fwd pass with fixed point quantization.

We can notice that although we use different analytical measurement for stochastic pruning (cosine similarity) and for quantization (relative error), both of them are "analytical related" and define normalize values for the distance between original and noised tensor. The use of relative error in floating point format was already used in previous works².

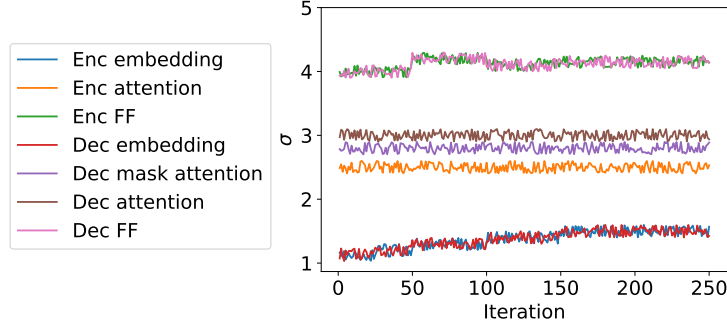


Figure A.7: (a) Std of layers gradient in different layers in the transformer (Vaswani et al., 2017) in WMT'16 En-De dataset assuming log-normal distribution. Notice the variability of std, which make the fp quantization challenging (Micikevicius et al., 2017).

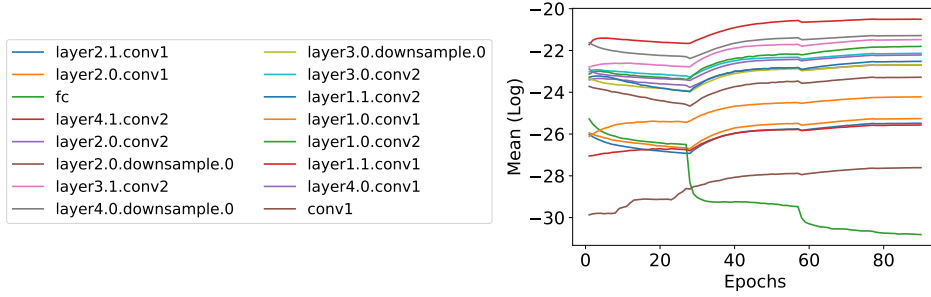


Figure A.8: Layer gradients means (log scale) in all layers of ResNet18, ImageNet dataset. Notice that the first ("Conv1") and last ("fc") suffer from a different statistic which requires a layerwise scaling factor.

A.12 Experiments

We implement all the experiments in PyTorch, models are trained on ImageNet dataset (Deng et al., 2009) and are evaluated on three different architectures ResNet18 (He et al., 2016), DenseNet121 (Huang et al., 2017) and VGG16 (Simonyan & Zisserman, 2015). We train the models with the standard regime for 90 epochs, using SGD with momentum, reducing the learning rate by a factor of $\frac{1}{10}$ after 30 and 60 epochs. Note the difference between the ATP and our homogeneous method is only the way to find the threshold α for a required sparsity. Therefore, we believe the difference in the accuracy for same sparsity (we had better results) is probably the result of implementation issues. Our heterogeneous method further improves the validation accuracy for a given sparsity level, as shown in Fig. 5. Lastly, we note that ATP (Ye et al., 2019) for some reason only reported training accuracy, but not to be too strict (it might have been just a typo) we assumed that their validation accuracy was the same as the training accuracy — as was in our experiments.

²Accuracy and Stability of Numerical Algorithms: Second Edition; Nicholas J. Higham

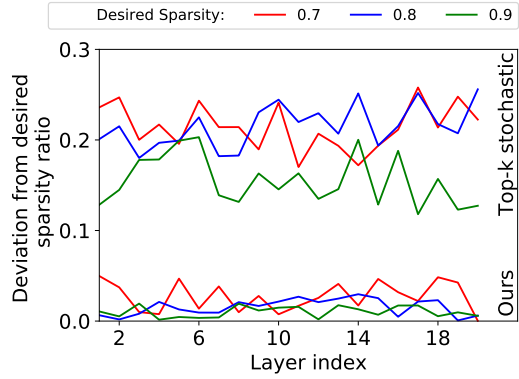


Figure A.9

Figure A.10: Comparison of the deviation from the desired sparsity ratio of stochastic pruning Vs "top-k" + stochastic pruning, i.e finding the threshold α with "top-k" and then applying stochastic pruning. (Eq. (3)) in different layers. Notice the high deviation in "top-k" + stochastic pruning is uniform across the layers

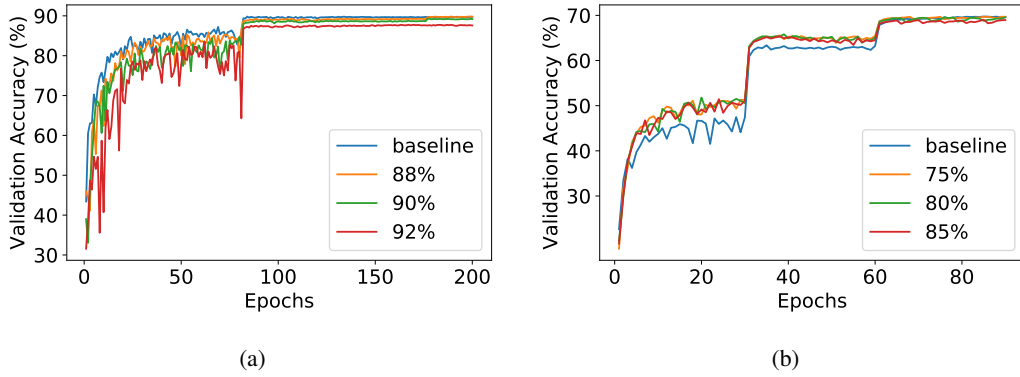


Figure A.11: ResNet18 training convergence with different sparsity ratios for Cifar10(a) and Imagenet(b) datasets.

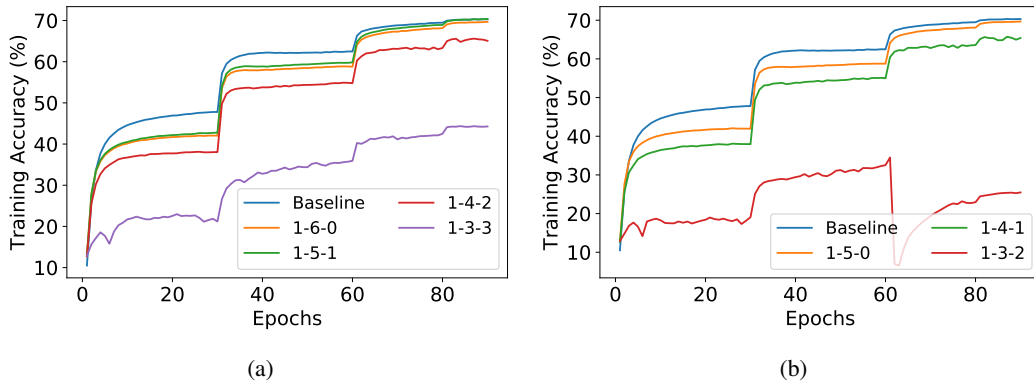


Figure A.12: FP7(a) and FP6(b) training convergence in different formats in ResNet18, ImageNet dataset. Notice the results fit the analysis in Fig. 4b

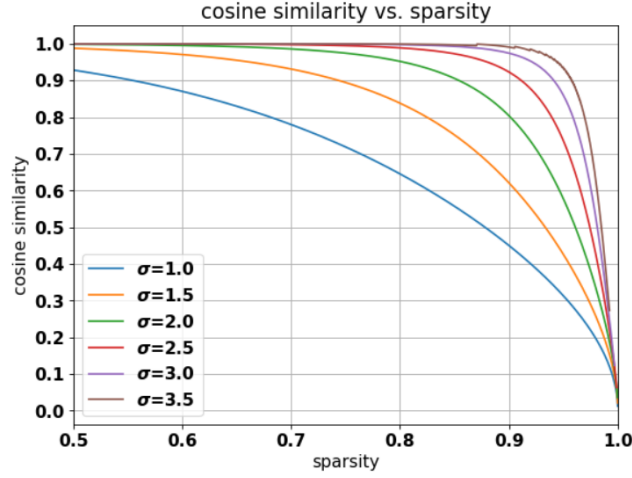


Figure A.13: Cosine similarity vs. sparsity for different σ . For all distributions plotted here $k = 2.5$. The values were calculated analytically using our analyses of the sparsity and cosine similarity using stochastic pruning. Notice that for the same sparsity values different distributions vary significantly in cosine similarity, this explains the difference in cosine similarity of the different layers when using homogeneous stochastic pruning (all layers having the same sparsity level).



Figure A.14: Actual sparsity of the different layers of ResNet18 trained on ImageNet using heterogeneous stochastic pruning. The desired sparsity was 92% and the overall achieved one is 91.5%, the minimum cosine similarity for blocks 3 & 4 was 0.98 and for block 2 was 0.95, and the maximum allowed sparsity for the rest of the layers (block 1 and "conv1" before the first block) was 0.98. Notice that the high sparsity levels was induced on the first block and "conv1", and that some of the layers, especially from block 2, had much lower sparsity levels in order to preserve its cosine similarity. For this experiment the validation accuracy was less than 1% degradation from baseline, compared to over 3% degradation for the homogeneous algorithm at similar sparsity level.

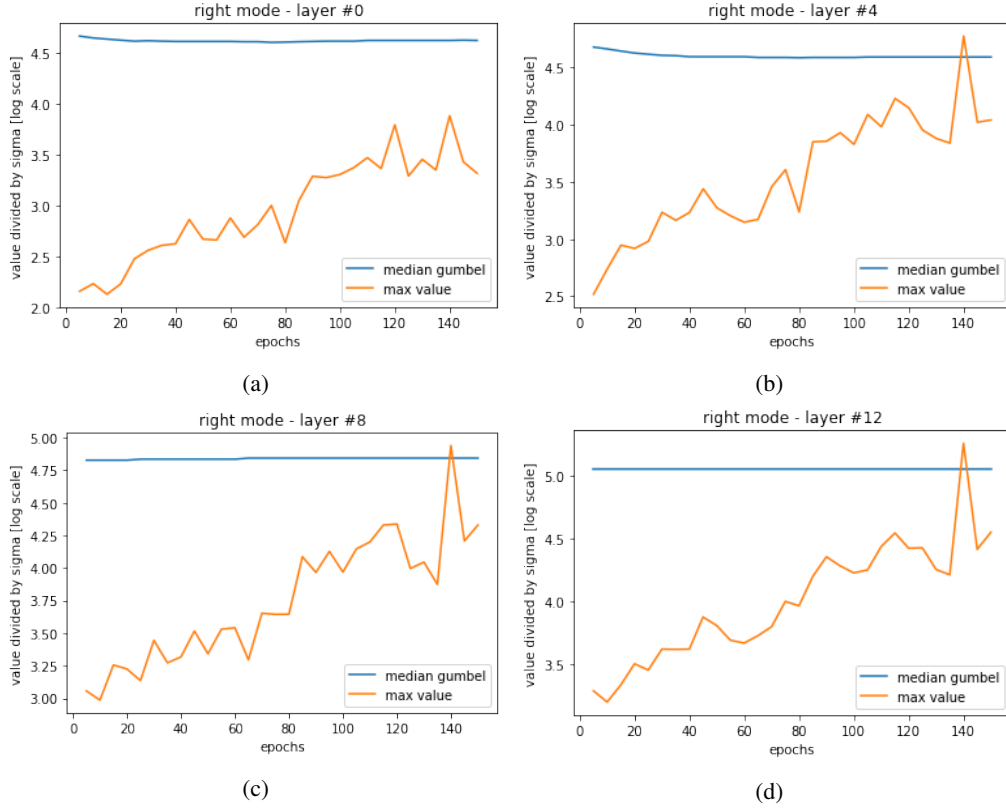


Figure A.15: Comparison between the median value of the Gumbel distribution and the actual maximum value of the gradients for ResNet18 trained on Cifar10. The Gumbel distribution represents the distribution of the maximum value for a tensor of the size of the gradients tensor (each layer of different size) drawn from a lognormal distribution with the mean and std of the tensor. Here we use only the right mode of the bi-modal mixture of lognormal distributions. Notice that the actual maximum value is orders of magnitudes lower than the expected maximum value from the Gumbel distribution (y-axis is in log scale, and the value is divided by the std). The actual tensors are truncated at levels of approximately $3-5\sigma$. This observation lead us to model the distribution as a truncated lognormal distribution when we derived the cosine similarity analytically, because the cosine similarity is more sensitive to the presence of high-valued components in the tensor. The numbering of the layers here is from the deepest to the shallowest, according to the order of the gradients flow in the backward-pass. Notice that layer 12 gradients has twice as many elements as layer 8 that has twice as many as layers 4 and 0, thus the median of their Gumbel distributions is higher, measuring in sigmas, because if we draw more values we expect the maximum value to be larger.

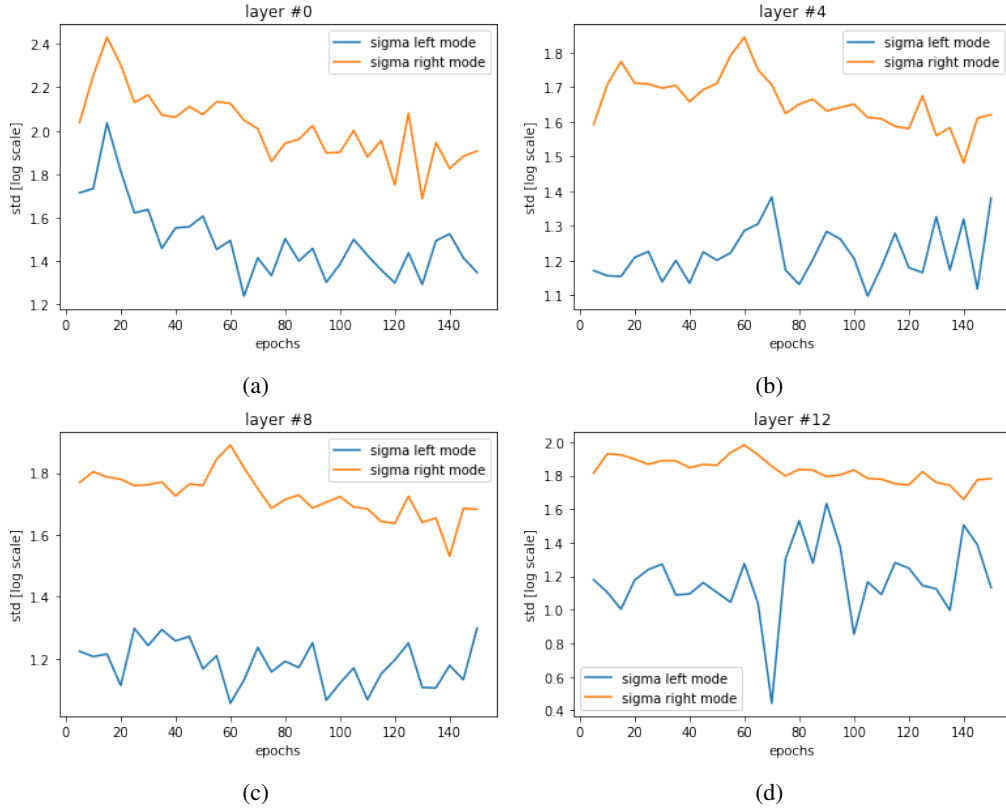


Figure A.16: The std (σ) of each of the two modes of the gradients for ResNet18 trained on Cifar10, on various layers. Notice that the left mode is of lower variance. The numbering of the layers here is from the deepest to the shallowest, according to the order of the gradients flow in the backward-pass.

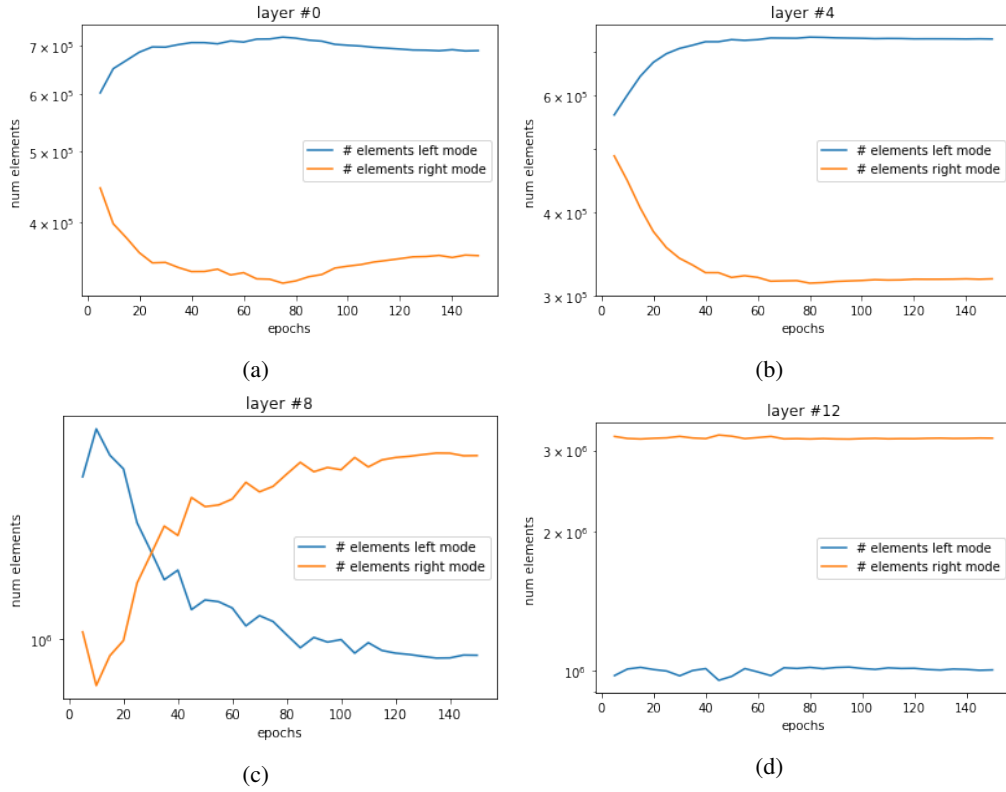


Figure A.17: The number of elements of each of the two modes of the gradients for ResNet18 trained on Cifar10, on various layers. Notice that the y-axis is in log scale. Different layers vary in behaviour, but the dominant effect is the increase in the proportion of the left mode, indicating that a large portion of the values are mapped to zero by the consequent ReLU layer, because the left modes' values originate from zeros values in the ReLU gradients. Up to 80% of values might be in the left mode. This has major consequences when trying to prune the bi-modal distributions to values lower than that using our algorithm. However this is less of a problem when pruning to high sparsity levels. The numbering of the layers here is from the deepest to the shallowest, according to the order of the gradients flow in the backward-pass.